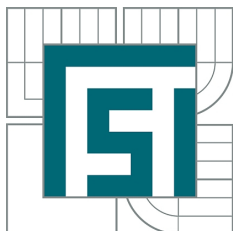


VYSOKÉ UČENÍ TECHNICKÉ V BRNĚ  
BRNO UNIVERSITY OF TECHNOLOGY



FAKULTA STROJNÍHO INŽENÝRSTVÍ  
ÚSTAV FYZIKÁLNÍHO INŽENÝRSTVÍ  
FACULTY OF MECHANICAL ENGINEERING  
INSTITUTE OF PHYSICAL ENGINEERING

STUDIUM VORTEXOVÝCH STAVŮ V MAGNETOSTATICKY  
SVÁZANÝCH MAGNETICKÝCH NANODISCÍCH  
SPIN VORTEX STATES IN MAGNETOSTATICALLY COUPLED MAGNETIC NANODISKS

DIPLOMOVÁ PRÁCE  
MASTER'S THESIS

AUTOR PRÁCE  
AUTHOR

Bc. MAREK VAŇATKA

VEDOUCÍ PRÁCE  
SUPERVISOR

Ing. MICHAL URBÁNEK, Ph.D.

BRNO 2015

Vysoké učení technické v Brně, Fakulta strojního inženýrství

Ústav fyzikálního inženýrství

Akademický rok: 2014/15

## **ZADÁNÍ DIPLOMOVÉ PRÁCE**

student(ka): Bc. Marek Vaňatka

který/která studuje v **magisterském studijním programu**

obor: **Fyzikální inženýrství a nanotechnologie (3901T043)**

Ředitel ústavu Vám v souladu se zákonem č.111/1998 o vysokých školách a se Studijním a zkušebním řádem VUT v Brně určuje následující téma diplomové práce:

**Studium vortexových stavů v magnetostaticky svázaných magnetických nanodiscích**

v anglickém jazyce:

**Spin vortex states in magnetostatically coupled magnetic nanodisks**

Stručná charakteristika problematiky úkolu:

Vortexy v magnetických nanodiscích jsou charakterizovány směrem stáčení magnetizace v rovině disku (cirkulací) a směrem magnetizace vortexového jádra (polaritou). Kombinací vzájemné orientace těchto charakteristik můžeme dosáhnout čtyř rovnocenných magnetických stavů, čehož je možné využít např. pro multibitové paměťové buňky.

Před praktickým využitím nanodisků jako paměťových buněk nebo jiných funkčních prvků spintronických zařízení je třeba provést studium přepínání vortexových stavů a následného vyčítání finálního stavu vortexu. Úkolem této diplomové práce je studium magnetostatické svázanosti dvojic (případně skupin) permalloyových nebo kobaltových nanodisků s řízenou asymetrií.

Cíle diplomové práce:

Proveďte rešeršní studii o problematice magnetických vortexů.

Prozkoumejte metody přípravy magnetických nanodisků s řízenou asymetrií.

Přípravené vzorky charakterizujte pomocí mikroskopie magnetických sil, magnetooptických a magnetotransportních měření.

Seznam odborné literatury:

- [1] Novosad, V. et al. Effect of interdot magnetostatic interaction on magnetization reversal in circular dot arrays. Phys. Rev. B 65, 060402 (2002).  
[2] Cui, X. et. al. Detection of a vortex nucleation position in a circular ferromagnet using asymmetrically configured electrodes Appl. Phys. Lett. 105, 082403 (2014).  
[3] Uhlíř, V. et. al. Dynamic switching of the spin circulation in tapered magnetic nanodisks. Nat. Nano. 8, 341-346 (2013).

Vedoucí diplomové práce: Ing. Michal Urbánek, Ph.D.

Termín odevzdání diplomové práce je stanoven časovým plánem akademického roku 2014/15.

V Brně, dne 21.11.2014



prof. RNDr. Tomáš Šíkola, CSc.  
Ředitel ústavu



doc. Ing. Jaroslav Katolický, Ph.D.  
Děkan

## Abstrakt

Magnetické vortexy ve feromagnetických discích jsou charakterizovány pomocí smyslu stáčení magnetizace v rovině disku a pomocí směru vortexového jádra kolmého k rovině disku. Bylo představeno několik konceptů paměťových médií využívajících magnetické vortexy, a ty jsou proto v současné době intenzivně studovány. Tato práce se zabývá magnetostatickým propojením dvojic magnetických disků, konkrétně objasněním jejich vzájemného ovlivňování v průběhu nukleačního procesu. Nejprve bylo třeba studovat náhodnost jednotlivých disků, abychom zajistili, že nově znukleovaný stav je ovlivněn pouze blízkými magnetickými strukturami. Prověřili jsme naše litografické možnosti za účelem dosažení nejlepší možné geometrie. Dále představujeme koncept elektrického čtení směru spinové cirkulace s využitím jevu anizotropní magnetorezistence. Tato metoda umožňuje automatické měření, čímž bylo umožněno získání dostatečně velkého statistického souboru. Byly také provedeny výpočty křivek magnetorezistence, abychom byli předem schopni analyzovat chování naměřených dat. Nakonec jsme provedli komplementární měření pomocí mikroskopie magnetických sil.

## Abstract

Magnetic vortices in ferromagnetic disks are curling magnetization structures characterized by the sense of the spin circulation in the plane of the disk and by the direction of the magnetization in the vortex core. Concepts of memory devices using the magnetic vortices as multibit memory cells have been presented, which brought the high demand for their research in many physical aspects. This work investigates the magnetostatic coupling in pairs of ferromagnetic disks to clarify the influence of nearby disks or other magnetic structures to the vortex nucleation mechanism. To ensure that the vortex nucleation is influenced only by the neighbouring magnetic structures, the randomness of the nucleation process was studied in single disks prior to the work on pairs of disks. We had to ensure that the vortex nucleation is influenced only by the neighbouring magnetic structures and not by an unwanted geometrical asymmetry in the studied disk. Lithographic capabilities were inspected in order to achieve the best possible geometry. Further we present a concept of electrical readout of the spin circulation using the anisotropic magnetoresistance, which allows automated measurements to provide sufficient statistics. To explain the magnetoresistance behaviour, numerical calculations together with magnetic force microscopy measurements are presented.

## Klíčová slova

magnetický vortex, přepínání cirkulace, magnetorezistence, mikroskopie magnetických sil.

## Keywords

magnetic vortex, circulation switching, magnetoresistance, magnetic force microscopy.

VAŇATKA, M. *Studium vortexových stavů v magnetostaticky svázaných magnetických nanodiscích*. Brno: Vysoké učení technické v Brně, Fakulta strojního inženýrství, 2015. 59 s. Vedoucí diplomové práce – Ing. Michal Urbánek, Ph.D.



PROHLÁŠENÍ:

Prohlašuji, že jsem diplomovou práci vypracoval samostatně pod odborným vedením Ing. Michala Urbánka, Ph.D., a že veškeré podklady, ze kterých jsem čerpal, jsou uvedeny v seznamu použité literatury.

Bc. Marek Vaňatka

## ACKNOWLEDGEMENT

I would like to express my gratitude to my supervisor **Dr. Michal Urbánek** for his kindness while staying late in the lab and for the leading of my project as well as the whole magnetism group at the Institute of Physical Engineering. I want to give my dearest thanks to **prof. Jiří Spousta** for proofreading of this thesis and for teaching me how to windsurf. I also thank **Lukáš Flajšman** and **Igor Turčan** for the help provided with the MFM and MOKE measurements and also for the atmosphere we made together in the lab to achieve decent research results. Many thanks belong to **Anna-Kay Russell** and **Cassandra Timmenga** not only for the language corrections, but also for the great company they made us in our Erasmus internship in Grenoble, France. I thank **Roman Jíra** for the help with the sample preparation and measurements and my greatest gratitude also belongs to **prof. Stefania Pizzini** for our Erasmus collaboration where I learned many great things. Last but not least I would like thank my family for their support during my whole life.

Part of the work was carried out with the support of **Nanofabrication and Nanocharacterization Core Facility of CEITEC** – Central European Institute of Technology under CEITEC – open access project, ID number LM2011020, funded by the Ministry of Education, Youth and Sports of the Czech Republic under the activity „Projects of major infrastructures for research, development and innovations”.

# Contents

<b>1</b>	<b>Introduction and Goals</b>	<b>2</b>
<b>2</b>	<b>Magnetic vortices in micromagnetism</b>	<b>4</b>
2.1	Basic relations in magnetism . . . . .	4
2.2	Energies at play . . . . .	5
2.3	Magnetization patterns at micro/nanoscale . . . . .	9
2.4	Vortex states . . . . .	9
2.4.1	Magnetization mechanism of a magnetic vortex . . . . .	10
2.4.2	Experimental methods for detecting magnetic vortices . . . . .	13
2.4.3	Applications of magnetic vortices . . . . .	14
2.5	Magnetostatic coupling in magnetic nanodisks . . . . .	15
<b>3</b>	<b>Lithography Methods – nanofabrication of magnetic disks</b>	<b>19</b>
3.1	Lift-off . . . . .	20
3.2	Ion beam etching using negative mask . . . . .	21
3.2.1	Resist masks . . . . .	21
3.2.2	Metal mask by positive lithography and lift-off . . . . .	23
3.3	Ion lithography by focused ion beam . . . . .	24
3.4	Wet chemical etching . . . . .	27
<b>4</b>	<b>Characterization methods</b>	<b>28</b>
4.1	Anisotropic magnetoresistance . . . . .	29
4.1.1	Detection of the vortex circulation by anisotropic magnetoresistance . . . . .	29
4.1.2	Experimental setup . . . . .	32
4.2	Magnetic force microscopy . . . . .	33
4.3	Magneto-optical Kerr effect . . . . .	34
<b>5</b>	<b>Results</b>	<b>35</b>
5.1	Simulations of anisotropic magnetoresistance . . . . .	35
5.2	Measurements of anisotropic magnetoresistance . . . . .	39
5.2.1	Measurements on single disks: a pursuit of randomness . . . . .	40
5.2.2	Pairs of disks . . . . .	44
5.3	Magnetic force microscopy . . . . .	45
5.4	Magneto-optical Kerr effect . . . . .	47
<b>6</b>	<b>Conclusion</b>	<b>49</b>
	<b>List of abbreviations</b>	<b>51</b>
	<b>Bibliography</b>	<b>52</b>

# Chapter 1

## Introduction and Goals

The first magnetic properties were discovered long before the Common Era (approximately the 5th century BCE), when humans observed the ability to attract ferrous objects by lodestones<sup>1</sup> – feeble permanent magnets that were magnetized by huge electric currents during lightning strikes [1]. Ever since, magnets have been attracting both people’s curiosity and scientific interest, but it has taken over two millennia to reach the most significant breakthroughs. The first of them was the unifying electromagnetic theory by James Clerk Maxwell in 1864 [2]. The following development of the micromagnetic theory by Langevin, Weiss, Heisenberg, Landau and others in the first half of 20th century further increased the understanding of magnets and magnetic ordering, by establishing the quantum mechanical foundation of magnetism [3]. The last and still ongoing milestone is the widespread of the magnetism applications through the recording media industry, which started with the computer era after World War II and rapidly accelerated in early 1990s with the discoveries of magnetoresistance effects used in modern hard disk drives [4]. Electronic devices no longer use only the electric charge to operate, but the novel concepts with patterned magnets also profit from the other fundamental magnetic property of an electron called spin. Therefore electronics using both the charge and the spin of an electron started to be called spin-electronics or simply spintronics.

The main applications of spintronics are in data storage, with the hard disk drives being its long lasting evergreen. Other concepts have been presented as well, including the racetrack memory [5] or magnetic random access memory (MRAM) [6]. Magnetic vortices, studied extensively at the Institute of Physical Engineering, Brno University of Technology (IPE BUT), have also been proposed to adopt the role of the recording media [7]. Furthermore, magnetic vortices can be utilized in logic circuits, random number generators or even in some biological applications.

Magnetic vortices are curling magnetization structures that represent the lowest energy state in (sub)micrometer sized magnetic disks or polygons. A vortex state is characterized by two parameters: the circulation of the magnetization in the plane of the disk and the polarity of the core magnetized perpendicularly to the disk surface. The combination of the two parameters allows for four possible configurations of circulation and polarity (vortex states),

---

<sup>1</sup>Rocks rich in  $\text{Fe}_3\text{O}_4$ .

which give rise to multibit memory cells in the considered storage media. Our research interest in the field of magnetic vortices spreads into the study of multiple aspects with the common goal of effective writing and readout of the vortex states towards a fast multibit memory device. Our group recently presented significant results about the dynamic switching of the vortex states in tapered nanodisks [8] and about the dynamical reversal with analytical modelling [9].

The goal of this work is to investigate the magnetostatic coupling in pairs of magnetic nanodisks made of Permalloy ( $\text{Ni}_{80}\text{Fe}_{20}$ ). The necessary premise to this investigation is that individual disks (without the presence of nearby magnetic structures) exhibit random behaviour in terms of nucleated polarity and circulation. If this was not fulfilled, any result would always be highly questionable – it would not be clear, whether the state is given by the stray fields of the neighbouring disk or by some other effects, mostly the geometrical asymmetry. The crucial parameter is the geometric quality of the disk, so our lithographic capabilities had to be explored. While vortices have the two mentioned parameters (polarity and circulation), we are only concerned with the vortex circulation, because the core size  $\sim 30\text{ nm}$  is not detectable in our magnetoresistance measurement method. To detect the vortex polarity, a much more complicated detection device fabricated by advanced lithography techniques would be required and it is not pertinent to this work. By measuring magnetoresistance in the presented concept of the circulation readout, we should be able to provide sufficient statistics ( $\sim 10\,000$  measurements) to prove either the randomness of a vortex state nucleation or the magnetostatic coupling in a pair of disks. In addition to the magnetoresistance method, magnetic force microscopy will be used as a useful complementary method, as it can visualize the magnetization of the vortex even with its core polarity. On the other hand, it can never provide sufficient statistic due to its slow scan speed (units of images per hour). Magneto-optical Kerr effect is not particularly convenient for probing  $\sim 1\text{ }\mu\text{m}$  disks due to the resolution limit, but it is used for some specific types of measurements like hysteresis loops.

This work is divided into 6 chapters. Following the introduction, Chapter 2 explains the essentials of micromagnetism: a theory for describing systems too large for purely quantum mechanical approach and too small to be addressed only by Maxwell's theory of electromagnetic fields. In the end of this chapter, vortex states are described, including the applications and some of the expected properties given by the magnetostatic coupling. Chapter 3 is devoted to the used lithography methods and to the possible approaches of the sample fabrication. They are important in reaching the essential randomness in the nucleation process, because the geometrical quality of the prepared disk is the crucial parameter. Chapters 4 and 5 are dedicated to the description of the used measurement methods (anisotropic magnetoresistance, magnetic force microscopy and magneto-optical Kerr effect) and to the presentation of achieved results. Finally, Chapter 6 summarizes the accomplished work and discusses the future outlook on this topic.

## Chapter 2

# Magnetic vortices in micromagnetism

The origin of magnetism lies within the relativistic quantum mechanics; therefore the problems should be treated accordingly by solving the many-body Schrödinger equation. However it is not only difficult, but for systems of micrometer sizes, it is also impossible due to the very limited computational resources available in 2015.

Micromagnetism is a theory bridging macro-sized objects, that are usually described by Maxwell's theory of electromagnetic fields, and nano-sized objects of pure quantum-mechanical treatment. This chapter describes the essentials of the micromagnetic theory. A detailed understanding would require studying more resources, for example [1, 10, 11].

### 2.1 Basic relations in magnetism

Unlike electrostatics, there are no isolated monopoles in magnetism. Instead, the basic elements are current loops – magnetic dipoles – characterized by a magnetic moment  $\vec{m}$  in units of  $A \cdot m^2$ . As a result of (relativistic) quantum mechanics, electrons are given with an intrinsic magnetic moment called a spin. Therefore the main magnetic effect in condensed matter originates from atoms with unpaired electrons, where the spins cannot compensate, namely in Fe, Ni and Co atoms. The volume density of magnetic dipoles is called magnetization, defined as

$$\vec{M} = \frac{\sum \vec{m}}{V}. \quad (2.1)$$

In vacuum, magnetic dipoles create a magnetic field  $\vec{H}$ . In material, magnetic induction  $\vec{B}$  is defined using the equation

$$\vec{B} = \mu_0 \vec{H} + \mu_0 \vec{M}. \quad (2.2)$$

Consequences of the relation (2.2) are demonstrated in Figure 2.1, which shows  $\vec{H}$  and  $\vec{B}$  fields in a homogeneously magnetized rectangle. The direction of the  $\vec{H}$  field inside of the magnetic material opposes the direction of  $\vec{B}$  and  $\vec{M}$  and is often called the demagnetizing field  $\vec{H}_d$ . Given by the Maxwell equation

$$\vec{\nabla} \cdot \vec{B} = 0, \quad (2.3)$$

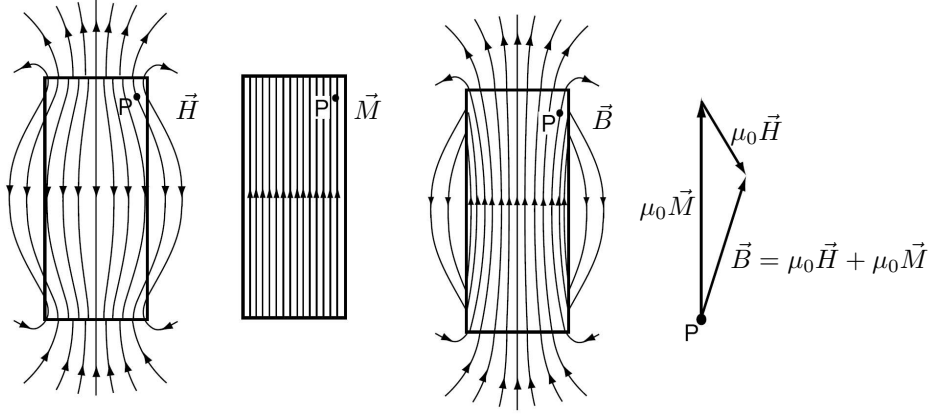


Figure 2.1:  $\vec{H}$ ,  $\vec{M}$  and  $\vec{B}$  vectors in a homogeneously magnetized rectangle have to fulfil the equation (2.2). In material,  $\vec{H}$  opposes the direction of  $\vec{M}$  and  $\vec{B}$  and is often called the demagnetizing field  $\vec{H}_d$  (taken from [1]).

$\vec{H}$  also has to be divergenceless in the free space, because  $\vec{B} = \mu_0 \vec{H}$ . But there is also no reason why  $\vec{H}$  and  $\vec{M}$  could not have sources, which leads to the concept of magnetic charges. By combining equations (2.2) and (2.3), we obtain

$$\rho_m = -\mu_0 \vec{\nabla} \cdot \vec{M} = \mu_0 \vec{\nabla} \cdot \vec{H}. \quad (2.4)$$

This equation is analogical with the electrostatic case, where  $\rho_e = \varepsilon_0 \vec{\nabla} \cdot \vec{E}$ .

Some energy relations in the following Section 2.2 are concerned only with the local direction of magnetization, not its magnitude, so it is also appropriate to define a unit vector pointing in the direction of magnetization:

$$\vec{m} = \frac{\vec{M}}{M_s} \quad (2.5)$$

where  $M_s$  is the saturation magnetization.

## 2.2 Energies at play

In general, the final magnetization state of a microstructure is a result of minimizing the total free energy, and it reflects either a local or an absolute energy minimum [1]. There are several contributions to the total energy:

$$\varepsilon_{\text{tot}} = \varepsilon_{\text{ex}} + \varepsilon_Z + \varepsilon_d + \varepsilon_a + \dots \quad (2.6)$$

The principal contributions are mainly exchange energy  $\varepsilon_{\text{ex}}$ , Zeeman energy  $\varepsilon_Z$ , dipolar energy  $\varepsilon_d$  and anisotropy  $\varepsilon_a$ . In some specific cases, other terms may be added; for example the Dzyaloshinski-Moriya interaction. Each of those contributions is usually given in the form of a volume integral and it is described in the following paragraphs.



## Exchange interaction

The coupling of the two spins  $\vec{S}_i$  and  $\vec{S}_j$  can be expressed through the exchange interaction, which is purely of the quantum mechanical origin. Its basic consequence is that the adjacent magnetic moments prefer to be aligned collinearly [12], expressed by the Heisenberg Hamiltonian [1, 10]:

$$\mathcal{H}_{\text{ex}} = - \sum_{i \neq j} \mathcal{J}_{ij} \vec{S}_i \cdot \vec{S}_j, \quad (2.7)$$

where  $\mathcal{J}_{ij}$  is the exchange constant with units of energy.  $\mathcal{J}_{ij}$  can be both positive and negative, where  $\mathcal{J}_{ij} > 0$  indicates a ferromagnetic interaction leading to parallel spin alignment and  $\mathcal{J}_{ij} < 0$  indicates an antiferromagnetic interaction preferring the antiparallel spin alignment [12].

In the approximation of continuous magnetization, the exchange energy can be expressed as an energy penalty

$$\varepsilon_{\text{ex}} = \iiint A [(\nabla m_x)^2 + (\nabla m_y)^2 + (\nabla m_z)^2] dV, \quad (2.8)$$

where the material constant  $A$  is the exchange stiffness coefficient in units of  $\text{J m}^{-1}$  and  $m_x, m_y, m_z$  are the components of the unit magnetization vector  $\vec{m}$  defined in the equation (2.5). The typical values are  $A = 13 \text{ pJ m}^{-1}$  for Permalloy and  $31 \text{ pJ m}^{-1}$  for cobalt [13].

In addition, we can calculate the exchange length [1]

$$l_{\text{ex}} = \sqrt{\frac{A}{\mu_0 M_s^2}} \quad (2.9)$$

describing the competition between the exchange energy (2.8) and the later mentioned dipolar energy (2.11). In a longer range than  $l_{\text{ex}}$ , the dipolar interaction has a larger influence and the exchange interaction becomes negligible. The exchange length values are  $4.0 \text{ nm}$  for Permalloy and  $3.5 \text{ nm}$  for Co (considering table  $M_s$  values  $800 \text{ kA m}^{-1}$  and  $1424 \text{ kA m}^{-1}$  respectively [14]).

## Zeeman energy

An external magnetic field  $\vec{H}_{\text{app}}$  submits the magnetization  $\vec{M}$  to a torque  $\vec{\Gamma} = \vec{M} \times \vec{H}_{\text{app}}$ , meaning that a misalignment of  $\vec{M}$  and  $\vec{H}_{\text{app}}$  leads to an energy increase:

$$\varepsilon_Z = -\mu_0 \iiint \vec{M} \cdot \vec{H}_{\text{app}} dV. \quad (2.10)$$

## Dipolar interaction

The dipolar energy has the same origin as the Zeeman energy, only the field is created by the magnetic moments themselves. As previously mentioned, this field is called the demagnetizing field  $\vec{H}_d$ . The energy term reads

$$\varepsilon_d = -\frac{1}{2} \mu_0 \iiint \vec{M} \cdot \vec{H}_d dV. \quad (2.11)$$

The factor  $\frac{1}{2}$  is introduced in order to avoid counting twice the interaction of moments A with B, and B with A [15].

Minimizing the dipolar energy leads to a reduction of the volume and surface magnetic charges, which is called the charge avoidance principle [1]. The sample shape (or the integration region) plays a crucial role here, often referred to as the shape anisotropy. However, the shape anisotropy is not related to other anisotropies like magnetocrystalline [13], which will be covered in the next section.

## Anisotropy

In a crystalline material, the magnetization aligns preferentially along certain crystallographic directions called easy axes: this is one of the aspects of the magnetic anisotropy which can be explained by the symmetry of the local environment [12].

In the simplest case of the uniaxial<sup>1</sup> anisotropy, found in hexagonal or orthorhombic crystals [13], the energy term is

$$\varepsilon_a = \iiint K_u \sin^2 \theta \, dV, \quad (2.12)$$

where  $K_u$  is the energy density of the uniaxial anisotropy and  $\theta$  is the angle between the easy axis and the vector of magnetization  $\vec{M}$ .

A strong anisotropy can be found in hard magnets, usually used for permanent magnets. In soft magnetic materials, such as Permalloy, the anisotropy is weak or even negligible.

## Other energy terms

Equation (2.6) shows four basic terms that are always present, but some other terms arise in specific cases of materials. Materials with low symmetry can exhibit weak antisymmetric coupling, the Dzyaloshinski-Moriya interaction (DMI), characterized by a vector  $\vec{D}$  and represented by the Hamiltonian [1]

$$\mathcal{H}_D = -\vec{D} \cdot (\vec{S}_i \times \vec{S}_j) \quad (2.13)$$

The corresponding energy equation is [16, 17]

$$\varepsilon_D = t \iint D \left[ \left( m_x \frac{\partial m_z}{\partial x} - m_z \frac{\partial m_x}{\partial x} \right) + \left( m_y \frac{\partial m_z}{\partial y} - m_z \frac{\partial m_y}{\partial y} \right) \right] dS. \quad (2.14)$$

where  $t$  is the layer thickness and  $D$  becomes a scalar value.

This DMI is not vanishing, for example in trilayers of Pt/Co/AlO<sub>x</sub> with an ultra-thin layer of Co ( $t < 1$  nm), where it forms a perpendicular magnetic anisotropy and Néel domain walls [18, 19]. DMI also gives rise to new, intensively studied magnetic quasiparticles called Skyrmions [17, 20].

Another weak, higher-order effect, sometimes detectable for the rare-earths, is the bi-quadratic exchange characterized by the constant  $\mathcal{B}$ , with its Hamiltonian [1]

$$\mathcal{H}_B = -\mathcal{B}(\vec{S}_i \cdot \vec{S}_j)^2. \quad (2.15)$$

Applied stress on a magnetic material will increase the total energy as well. With the use of Permalloy, only the four basic terms of (2.6) have to be taken into account, while we

---

<sup>1</sup>Uniaxial means having only one easy axis.

can often neglect the very weak anisotropy. When no external magnetic field is applied, the magnetization state will be the result of competing the exchange and dipolar interactions.

### Magnetization dynamics

In an equilibrium state (at the energy minimum), the magnetization is parallel to the local effective field given by [1]

$$\vec{H}_{\text{eff}} = -\frac{1}{\mu_0} \frac{\partial \varepsilon_{\text{tot}}}{\partial \vec{M}} \quad (2.16)$$

and the torque acting on magnetization vanishes:

$$\vec{M} \times \vec{H}_{\text{eff}} = \vec{0}. \quad (2.17)$$

A model for evolution of the magnetization vector in time is given by the Landau-Lifshitz-Gilbert (LLG) equation [21]:

$$\frac{\partial \vec{M}}{\partial t} = -\gamma \vec{M} \times \mu_0 \vec{H}_{\text{eff}} + \frac{\alpha}{M_s} \left( \vec{M} \times \frac{\partial \vec{M}}{\partial t} \right), \quad (2.18)$$

where  $\gamma = \frac{e}{2m_e}$  is the gyromagnetic ratio and  $\alpha$  is the phenomenological damping constant. Figure 2.2 shows solved trajectories of the magnetization vector for both cases with and without damping  $\alpha$  included in the equation (2.18).

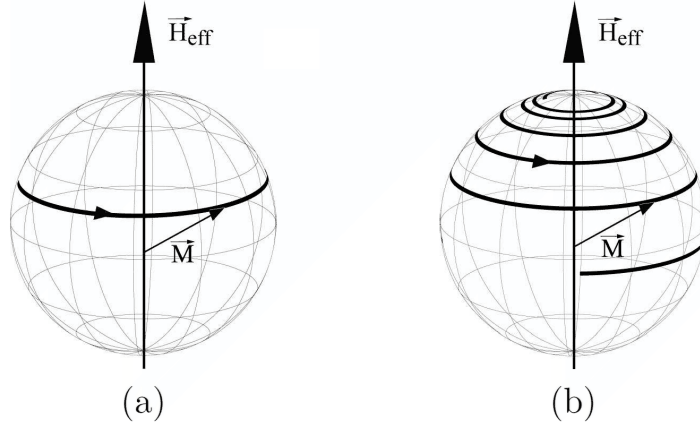


Figure 2.2: Dynamics of a magnetization vector. (a) No damping: the magnetization vector precesses around the direction of  $\vec{H}_{\text{eff}}$ . (b) Non-zero damping: magnetization is spiraling to the equilibrium position due to the energy dissipation (taken from [12]).

### Numerical micromagnetic simulations

When calculations of magnetization states in 3D magnetic bodies are done numerically, two approaches can be employed:

- finding a minimum of the energy functional (sum of all energy contributions),
- numerical integration of the LLG equation (2.18).

The volume of magnetic material has to be discretized into small cells, where the magnetization direction is assumed to be constant. Two main approaches include the finite difference method (cube cells) and the finite element method (tetrahedra cells). For both methods, there are several public or commercial codes for solving micromagnetic problems, with specific examples of the free codes:

- **Object Oriented Micromagnetic Framework (OOMMF)**

A public micromagnetic solver from NIST<sup>2</sup> [22], finite difference method. The oldest and also the most commonly used code.

- **MuMax**

A free graphic-card accelerated solver also using the finite difference method [23].

- **NMag**

Finite element method solver with problem description in the Python programming language [24].

- **MagNum**

Finite element method solver capable of using both graphic card and processor unit [25].

## 2.3 Magnetization patterns at micro/nanoscale

Very small nanoparticles ( $\sim 10$  nm) remain in a single domain state [26]. On the other hand, bulk materials break into a very high number of rather complex magnetic domains: areas with uniform direction of magnetization. In between those two scales, for example in patterned thin layers with lateral sizes of few microns, magnetization can break into just a few simple magnetic domains. Interesting magnetization structures like Landau patterns [27], spin ices [28], Skyrmions [20] or magnetic vortices may be formed. Magnetic force microscopy (MFM) is a common technique capable of probing the magnetization structure, some examples of these patterns are shown in Figure 2.3.

A continued discussion on magnetic vortices follows as they are the subject of this work. Many useful insights about domains in general can be found in an excellent book entitled *Magnetic Domains* by A. Hubert [3].

## 2.4 Vortex states

Minimizing the dipolar energy can lead to flux closing structures, where the surface magnetic charges are eliminated. The formed structures are called magnetic vortices and may be found in magnetic disks and polygons made from magnetically soft materials, the most frequently used material is Permalloy (an alloy of 80 % Ni and 20 % Fe). The main interest is given to vortices in magnetic disks, that can possess four degenerate states. Two degrees of freedom may be described by the independent parameters:

---

<sup>2</sup>National Institute of Standards, Gaithersburg, USA.

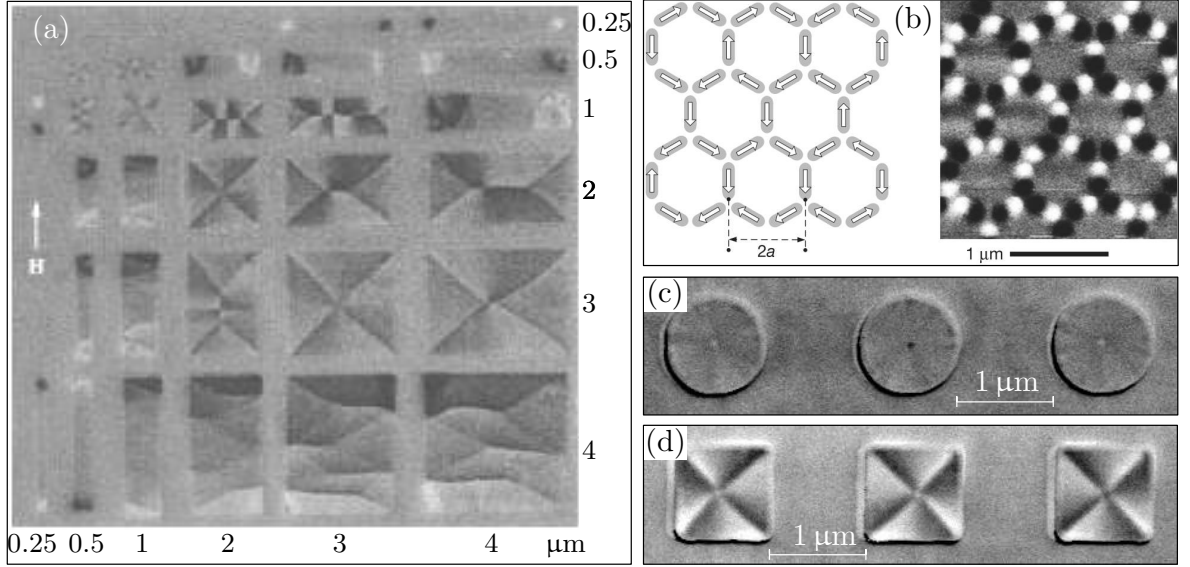


Figure 2.3: Magnetic force microscopy images of magnetization structures in Permalloy patterns. (a) Multidomain states in micron sized rectangles and squares [29]. (b) Spin ice formed in hexagonals built up from isolated rods [30]. (c) Vortex structures in Permalloy disks, the white or black dots indicate the core polarity up or down respectively. (d) Landau patterns in Permalloy rectangles.

- **circulation** of the magnetization in the plane of the disk, curling either counterclockwise  $c = +1$  or clockwise  $c = -1$ ,
- **polarity** of the vortex core, pointing either up  $p = +1$  or down  $p = -1$ .

The combination of polarity and circulation defines chirality (handedness) of a vortex. A visualization of the four vortex states is shown in Figure 2.4. The degeneration of those states is conditional by the system having a perfectly symmetric geometry. This is one of the main problems of this work, as a certain level of asymmetry is always present in every lithographic method. When the geometry is not perfect, the place of the core nucleation is not random, but it is defined by the asymmetry and the vortex states are no longer degenerate. In some cases it is advantageous that we can control the nucleated vortex states by including a defined asymmetry into the disk [8], while it is undesired in some other cases, for example in random number generators [31].

#### 2.4.1 Magnetization mechanism of a magnetic vortex

The nucleation of the vortex states has its own mechanism. After having a saturated magnetic disk, vortices can nucleate when the magnetic field is decreased under the nucleation field  $B_{\text{nuc}}$ . Then the vortex core appears on the disk boundary and moves into a new equilibrium position. The nucleation is usually foregone through the formation of a metastable *C*-state [33, 34], where the moments are aligned into the shape of the letter *C* or even through an *S*-state where the spins are bent even more into similar shapes like the letter *S* (shown in Figure 2.5). Some literature considers the *S*-state to be spin instabilities obtained only in

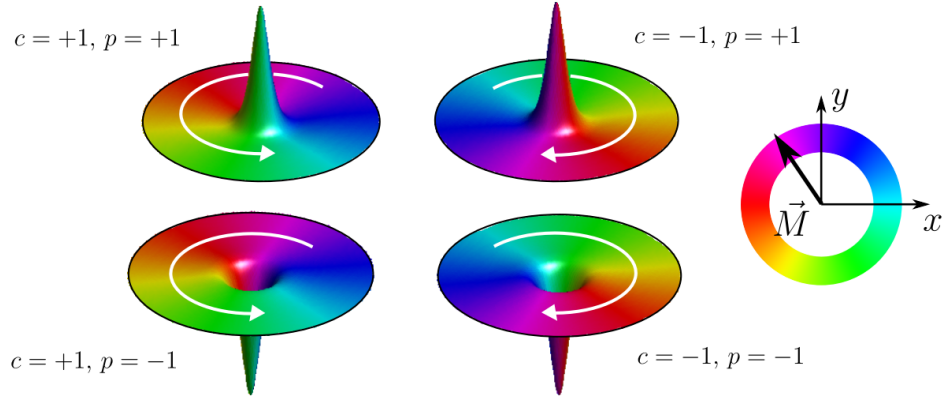


Figure 2.4: Visualization of the four possible vortex states, described by parameters circulation  $c$  and polarity  $p$  (taken from [32]).

micromagnetic simulations [35], but their presence in real systems was experimentally verified; the results are presented in Section 5.4. The intuitive formation of  $C$ -states in symmetric and asymmetric disks is shown in Figure 2.7.

When we apply a magnetic field to a disk with magnetization in a vortex state, the vortex core is pushed towards the disk perimeter to increase the average magnetization component along the field. After exceeding the annihilation field  $B_{\text{an}}$ , the vortex state disappears into saturation.

The vortex magnetization process possesses a specific hysteresis loop shape reflecting the magnetization mechanism explained above. An example of a typical magnetization loop (hysteresis) is shown in Figure 2.6.

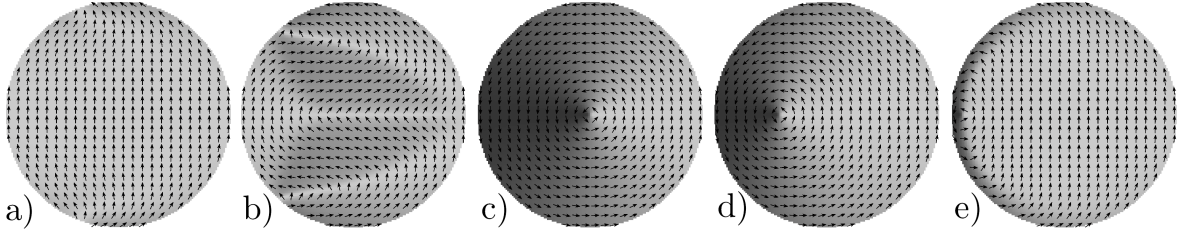


Figure 2.5: Micromagnetic simulation of a)  $C$ -state, b)  $S$ -state, c) vortex state at zero field, d) displaced vortex and e) vortex state right before annihilation; calculated in Object Oriented Micromagnetic Framework (OOMMF).

The response to the external field can be described by the analytical model called the rigid vortex model (RVM). It was previously derived in [36, 37] and it was also previously analyzed in the master's thesis defended at IPE BUT by Jan Balajka [32].

The disk of the radius  $R$  and the thickness  $L$  is described by a position vector in polar coordinates  $r$  and  $\varphi$ . Then the disk is divided into two regions: inside and outside of the vortex core described by the radius  $a$ , estimated as [36]

$$a = \left( \frac{\sqrt{2} l_{\text{ex}} L}{12\kappa} \right)^{\frac{1}{3}}, \quad (2.19)$$

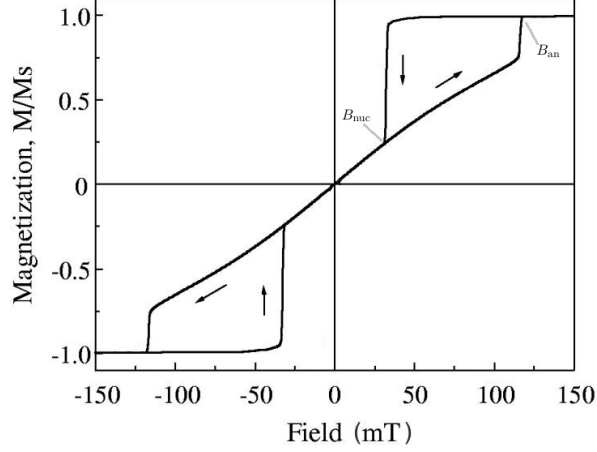


Figure 2.6: A typical vortex magnetization loop (adapted from [35]).

where  $\kappa \doteq 4.12 \cdot 10^{-2} \text{ m}^{-1}$  is a numeric constant. With the polar coordinates  $r$  and  $\varphi$ , the distribution of magnetization direction is given by [36]:

$$\text{for } r < a \begin{cases} m_x = \frac{-2ar}{a^2+r^2} \sin \varphi \\ m_y = \frac{-2ar}{a^2+r^2} \cos \varphi \\ m_z = \sqrt{1 - \left(\frac{-2ar}{a^2+r^2}\right)^2} \end{cases} \quad \text{for } a < r < R \begin{cases} m_x = -\sin \varphi \\ m_y = \cos \varphi \\ m_z = 0 \end{cases} \quad (2.20)$$

Further, RVM gives the core displacement  $l$  perpendicular to the applied field  $B$  using the initial magnetic susceptibility  $\chi(0)$ :

$$l = \chi(0) \frac{B}{\mu_0 M_s} R, \quad (2.21)$$

where the susceptibility was calculated by Guslienko et al. [37]:

$$\chi(0) = \frac{2\pi}{\frac{L}{R} \left[ \ln \left( \frac{8R}{L} \right) - \frac{1}{2} \right]}. \quad (2.22)$$

The annihilation field  $B_{\text{an}}$  may be calculated considering the core displacement  $l = R$ :

$$B_{\text{an}} = \frac{1}{\chi(0)} \mu_0 M_s. \quad (2.23)$$

The mean value of magnetization (in the disk volume  $V$ ) in the direction of the applied field is given as

$$\langle M \rangle_V = \chi(0) \frac{B}{\mu_0}. \quad (2.24)$$

A vortex is also not formed for all geometries, the single domain configuration is also possible. A phase diagram was previously simulated by J. Balajka [32] for disks of small diameters. It is shown in Figure 2.8.



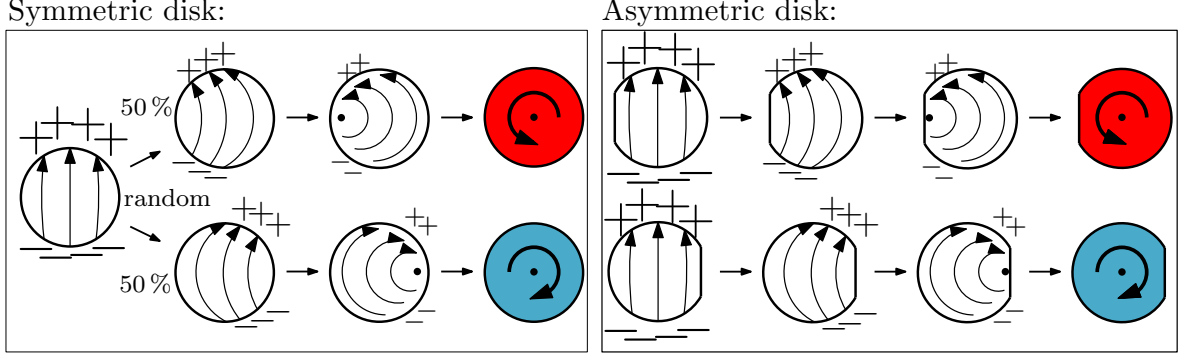


Figure 2.7: Schematics of the nucleation process of a vortex state in a symmetric disk (left) and in an asymmetric disk (right). The magnetic field decreases from left to right. While reducing the field, magnetization goes from saturation to a *C*-state. For magnetic field in the vertical direction, the *C*-state is formed either on the left or the right side of the disk – the side is random for a symmetric disk or defined by the asymmetry position for a tapered disk. After reaching the nucleation field  $B_{\text{nuc}}$ , a vortex core appears on the asymmetry. The final vortex state is formed when the field is completely turned off.

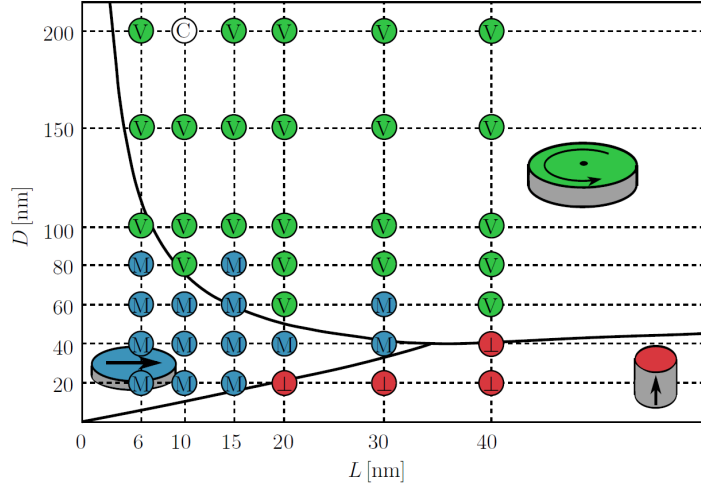


Figure 2.8: A simulated phase diagram for circular nanodots with diameter  $D$  and thickness  $L$ . Very small disks tend to form the monodomain state, either in-plane (denoted M) or out-of-plane (denoted  $\perp$ ). Vortex states (denoted V) are reached for a suitable combination of the diameter and thickness. One of the simulations ended in a metastable *C*-state, denoted C. The diagram was simulated by OOMMF (taken from [32]).

#### 2.4.2 Experimental methods for detecting magnetic vortices

In all of the electronic applications, effective writing and readout of the vortex states must be achieved. So far, several methods have been developed. For writing (switching) of the vortex states, the following methods have been used:

- Circulation switching by saturating the disk either by **static** [38] or **pulsed** [8] magnetic field and renucleating the core on a geometric asymmetry of the disk.
- Polarity toggling by small amplitude **in-plane alternating magnetic field** was shown

on Permalloy rectangles [39] and on Permalloy disks [40]. Toggling was also achieved by applying **in-plane pulses** [41, 42].

- Polarity switching by **in-plane rotating magnetic field** was presented in [43].
- Polarity switching by applying a **strong out-of-plane magnetic field** [44].

For the readout of vortex states, we have the following possibilities:

- **Magnetic force microscopy** (MFM) is a method utilizing the atomic force microscope with a magnetic to probe stray fields around nanostructures; it is especially useful for imaging the vortex cores [45, 46].
- **Lorentz microscopy** uses a transmission electron microscope, while the imaging is based on the electron deflection caused by the Lorentz forces [38, 47, 48].
- **Scanning electron microscopy with polarization analysis** (SEMPA) is a method implemented into an ultra-high vacuum scanning electron microscope with a spin-polarization detector of secondary electrons (spin polarized low energy electron diffraction or the Mott-detector) [49–51].
- **Magneto-optical Kerr effect** (MOKE) uses light for probing magnetic structures, the method’s resolution is restrained by the diffraction limit of light [52].
- **X-ray magnetic circular dichroism** (XMCD) uses synchrotron radiation for probing magnetization structures with  $\sim 25$  nm resolution and it is usually used to carry out time-resolved experiments [8, 53, 9].
- **Magnetic tunnel junctions** have been used to probe the core polarity; the downside is the requirement of advanced lithography techniques for the sample fabrication [54].
- **Anisotropic magnetoresistance** have been used to read the vortex circulation using either four point [48, 55, 56] or two point [57, 58] arrangement.

Only the last two methods are the possible candidates for practical applications due to the complexity of all the previous methods and the sizes of measurement setups.

### 2.4.3 Applications of magnetic vortices

Magnetic vortices have been studied for over a decade and several applications have been presented during that time. We can divide them into the following categories:

- **Multibit memory cells** in high density data storage [7, 59] are probably the most perspective application because of their non-volatility and high writing speed limits in order of GHz.
- **Radio-frequency devices** using the vortex core as an oscillator with geometry-dependent eigenfrequencies in the range from tens of MHz to units of GHz [60].

- **Logic circuits** may be developed as it was presented on an example of a XOR gate in [61].
- **Transistor operation** was shown on triads of vortices with controlling the amplification of the vortex core gyration by changing the polarity of the middle vortex [62].
- The concept of a **random number generator** is studied at IPE BUT using the randomness of the vortex circulation process [31].
- **Biological applications** have been presented as well, including a possibility for cancer treatment [63, 64].

## 2.5 Magnetostatic coupling in pairs and arrays of magnetic nanodisks

As it was described above, the magnetization process of a magnetic vortex follows the external magnetic field. The field is usually generated by external coils, electromagnets or waveguides, however it can also originate in the stray fields of the nearby magnetic structures. In nanopatterned samples, the stray fields surrounding the structures are small, but not negligible when we densely pack the objects. Previous research was given to magnetostatically coupled disks from the following aspects:

- The nucleation and annihilation fields were inspected as a function of the disk spacing (the field was applied along the rows of disks) with analytical description and magneto-optical measurements. It was found that both nucleation and annihilation fields decrease when the disks are placed closer together, as it is shown in Figure 2.9 [35, 52].
- Anihilation field difference with the core annihilation taking place either inside or outside of a pair of tapered disks ( $D = 1\ \mu\text{m}$ ,  $L = 40\ \text{nm}$ ) was measured using anisotropic magnetoresistance, Figure 2.10 shows that the annihilation field is higher when the vortices annihilate on the outer side of the pair [65].
- Simulations of the annihilation field difference in pairs of symmetric disks ( $D = 200\ \text{nm}$ ,  $L = 20\ \text{nm}$ ) were carried out in [32]. The results presented in Figure 2.12 are in disagreement with the previous point as the annihilation field on the inner side of the pair is higher than on the other side.
- High frequency vortex core gyration in pairs or arrays of disks was studied in references [66–71].
- Nucleated vortex circulations was measured by XMCD as a function of the disk spacing in arrays of  $1\ \mu\text{m}$  tapered Permalloy disks. The results show that the same or opposite circulations of the neighbouring disks depend on the interdisk distance, while small and large distance result in the same circulations and intermediate distance  $500\ \text{nm}$  results in identical circulations.[53]

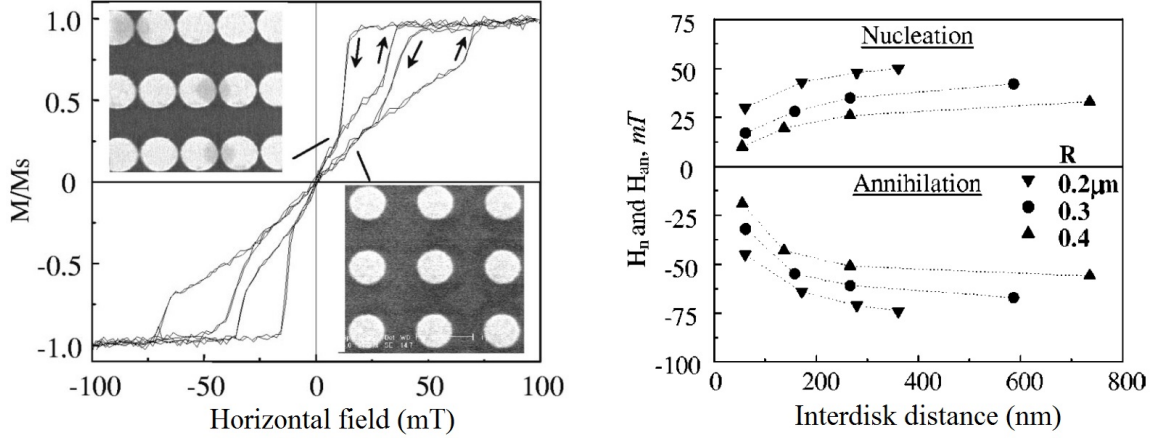


Figure 2.9: Left: Hysteresis loops of arrays of disks with different interdisk distance in the horizontal direction. When the disks are closer, both nucleation and annihilation field decrease. Right: Measured nucleation and annihilation fields for various disk radii (taken from [52]).

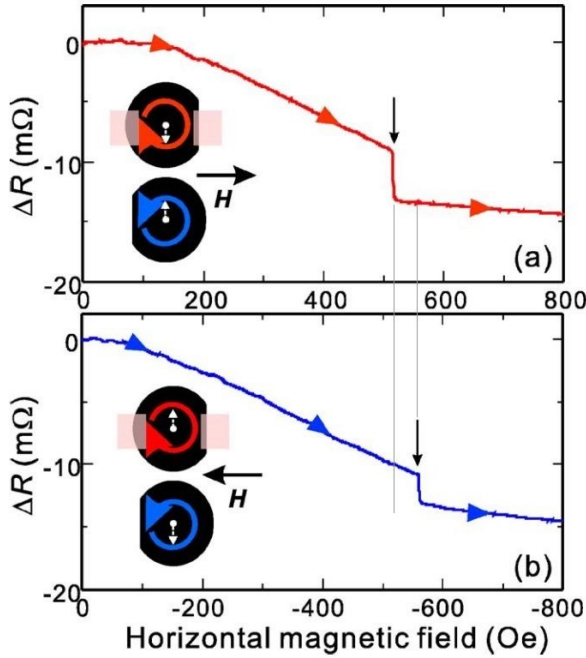


Figure 2.10: Measurement of the annihilation fields in a pair of tapered disks ( $D = 1 \mu\text{m}$ ,  $L = 40 \text{ nm}$ ) with opposite circulations. The disk is saturated in higher field when the annihilation takes place on the outer side of the pair of disks and earlier on the inner side. This data is in disagreement with the simulations carried out in [32] (taken from [65]).

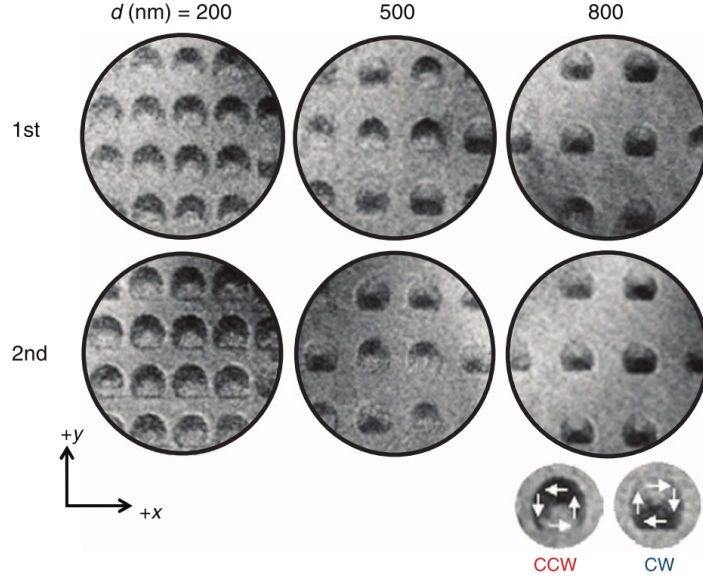


Figure 2.11: XMCD images of arrays of  $1\text{ }\mu\text{m}$  disks with various spacing. The circulations are the same for spacing 200 nm and 800 nm and opposite for spacing 500 nm (taken from [53]).

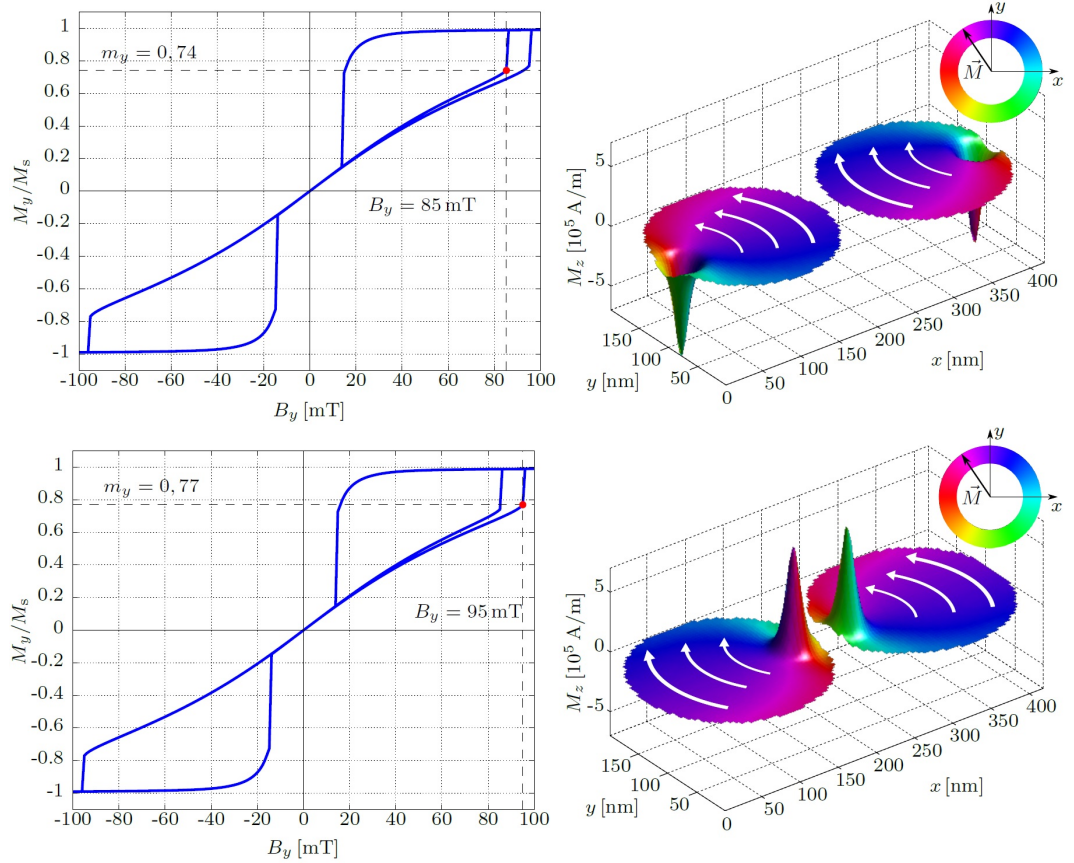


Figure 2.12: Simulation of the annihilation fields in symmetric disks with opposite circulations. The disk is saturated in higher field when the annihilation takes place on the outer side of a pair of disks and earlier on the inner side. This simulation is in disagreement with the data measured in [65] (taken from [32]).

The concept proposed in this project hypothesizes that pairs of geometrically symmetric magnetic disks will nucleate with opposite circulations. An explanation for this is that the vortex nucleation is foregone by formation of opposite  $C$ -states due to the charge repulsion as shown in Figure 2.13. This should stabilize opposite senses of magnetization rotation (opposite vortex circulations). The critical presumption for this experiment is that there is no other stronger effect influencing the vortex nucleation, especially a disk asymmetry (see Figure 2.7). It can be verified by the presence of randomness in the nucleation process, usually established by the perfect circular geometry of the studied disk. The best possible geometry will be pursued by the lithography methods described in the following chapter, Chapter 3.

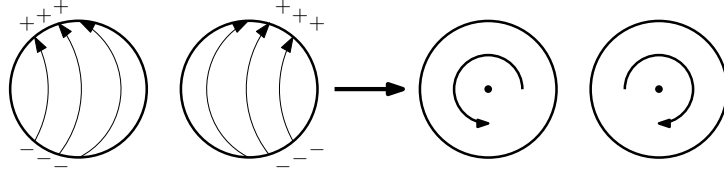


Figure 2.13: Schematics of the presented concept of vortex nucleation in a pair of symmetric disks. Before the nucleation, opposite  $C$ -states are formed, because identical charges repulse each other. Then the nucleated circulations are going to be opposite for each disk.

## Chapter 3

# Lithography Methods – nanofabrication of magnetic disks

The main challenge with this project was to fabricate samples consisting of magnetic disks or pairs of disks suitable for experimental studies of the magnetostatic coupling. The main requirement is randomness of the vortex states upon nucleation. Nucleation of a vortex state takes place as the vortex core appears on the edge of the disk, which is a random process considering a perfectly symmetrical geometry is present. By using any of the lithography methods, there is always a certain level of the edge roughness relying on many of the process parameters. The resulting question is: How perfect does the disk have to be to ensure the randomness of the nucleation process? This chapter discusses our current nanofabrication capabilities in order to achieve the best possible randomness of the vortex nucleations. Some proposals for further improvement are provided as well.

The basic lithography steps are briefly shown in Figure 3.1. A layer of resist (a substance sensitive to electrons or light) is spin-coated onto a clean substrate, usually a silicon wafer. The layer is then irradiated and developed. There are two possible procedures:

1. The **positive process** uses a positive-tone resist and the exposed parts are dissolved during the development.  
*example:* polymethyl methacrylate (PMMA)
2. The **negative process** uses a negative-tone resist and the exposed parts remain on the substrate after the development.  
*example:* SU-8<sup>1</sup>

The substrates with patterned resist are further processed as it is described in the following sections. Further details about lithographic procedures may be found in books [72, 73] or in master's and bachelor's theses previously defended at IPE BUT [74–76]. All scanning electron microscope (SEM) images were acquired with TESCAN Lyra3 electron microscope/focused ion beam system – the same instrument that was also used for all electron beam (e-beam) resist exposures and focused ion beam milling processes.

---

<sup>1</sup>Manufactured by MicroChem, <http://www.microchem.com>.



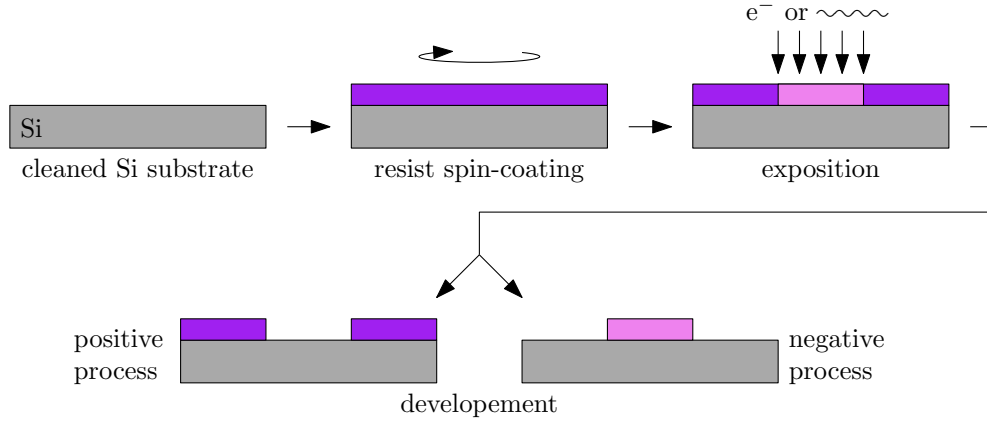


Figure 3.1: Schematics of a mask fabrication process. A resist layer is spin-coated onto clean substrates, usually silicon wafers. The samples are then exposed by electrons or by photons and developed. The process can be either positive (exposed parts are dissolved) or negative (exposed parts remain).

### 3.1 Lift-off

This technique is the simplest way to obtain patterns, but it always contains irremovable edge defects. After exposure and development of the resist layer, the material of interest is sputtered or evaporated onto the sample, as shown in Figure 3.2. We use an ion beam sputtering apparatus (described in [77, 78]), which is very directional compared to magnetron sputtering or evaporation. In our setup, however, it is not possible to align the substrate fully perpendicular to the ion beam direction, therefore two effects take place. Some areas of the substrate are shadowed by the resist layer and the metal atoms cannot land there, this effect is called shadowing. On the opposite edge, the metal is deposited on the side of the resist layer and it cannot be lifted off. An example of this problem is shown in Figure 3.3 and can be partially solved by using an undercut resist layer. In e-beam lithography, this can be achieved by using two layers of resist, where each of them need a different exposure dose, typically PMMAs with varying molecule lengths. This is unfortunately not possible in our conditions due to the lack of suitable resists. In photo-lithography, some available resists exhibit undercut profile directly after the development process, but it cannot be used for patterning submicron structures.

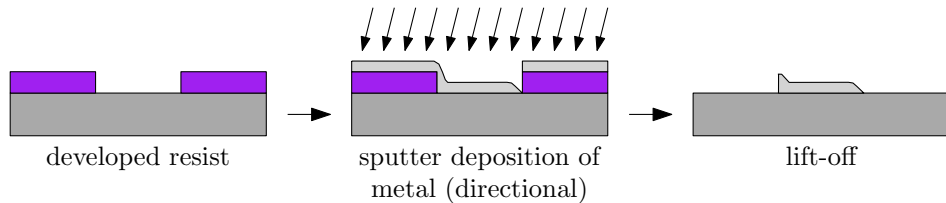


Figure 3.2: Schematics of the lift-off process. Metal is sputter deposited (or evaporated) onto the resist and substrate surface. The resist layer is dissolved in acetone and washed away along with the metal covering it. The remaining patterns on the substrate are usually asymmetric, because the deposition is usually directional and not perpendicular to the surface.

The resist layer is then stripped along with the metal layer on top of it, the rest remains on the substrate forming the desired patterns. The basic solvent for the most common e-beam resist, polymethyl methacrylate (PMMA), is acetone. Alternatives, such as Remover PG<sup>2</sup>, can also be used.

On the upside, the lift-off process can be used to fabricate tapered structures using shadowing effect. For example, by tapering magnetic disks, the direction of the nucleated vortex circulation can be controlled because the core preferentially nucleates on the tapered side of the disk. Nonetheless the desired symmetric patterns cannot be achieved.

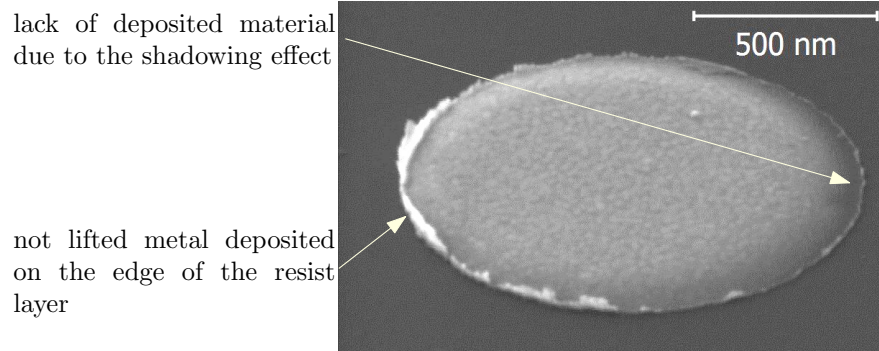


Figure 3.3: SEM image demonstrating the lift-off technique effects. Sample tilted to 55°.

## 3.2 Ion beam etching using negative mask

In the ion beam etching (IBE) process, an ion resistant mask is prepared on the top of a layer which is to be patterned. Then the metal can be etched (sputtered) away from the surface of the sample by ions (mostly  $\text{Ar}^+$ ) with energies in order of hundreds of eV. The mask can be either metallic (prepared by positive lithography and lift-off), or there are resists suitable for direct use as ion etching masks as described in the two following sections.

### 3.2.1 Resist masks

A schematics of a process using a resist mask is shown in Figure 3.4. The most suitable negative-tone e-beam resist for IBE is hydrogen silsesquioxane<sup>3</sup> (HSQ). During the exposure, HSQ is transformed into silicon dioxide ( $\text{SiO}_2$ ), characterized by good etching resistance. It also has a very good resolution, in best cases  $< 10\text{ nm}$ . Aqueous solutions of tetramethylammonium hydroxide (TMAH) or sodium hydroxide (NaOH) are often used as developers. The exposition doses vary widely with the development process and pattern sizes. For the processes using low doses ( $< 1000\ \mu\text{C}/\text{cm}^2$ ), an extra electron irradiation can be used in order to fully finish the transformation into  $\text{SiO}_2$  and to improve the etching resistance. After finishing the IBE process, the remaining mask can be easily dissolved in hydrofluoric acid (HF).

<sup>2</sup>Manufactured by MicroChem, <http://www.microchem.com>.

<sup>3</sup>Manufactured by Dow Corning, <http://www.dowcorning.com>.

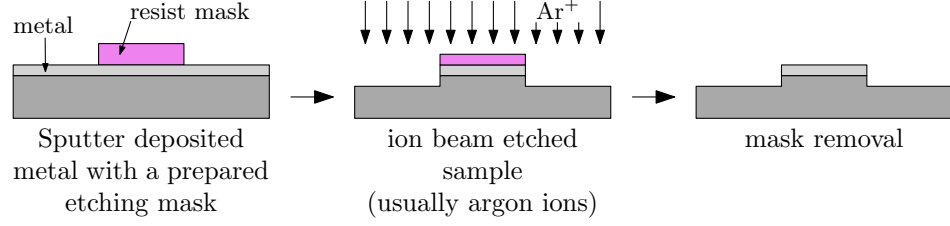


Figure 3.4: Schematics of the ion beam etching process using a resist mask. The patterned layer is sputtered away and the remaining mask is chemically removed.

The downside to this method is a very short shelf life of only 6 months and high price of the HSQ resist. There are also known adhesion problems on many metals, which can be dealt with by surface chemical modification, for example using (3-Aminopropyl) triethoxysilane (APTES) [30]. HSQ proved to have a good adhesion on Permalloy, surface modification by APTES did not bring any improvements.

Despite the promising characteristics of HSQ resist, we did not overcome the difficulties before the deadline, shut down of the IBE apparatus also delayed our work. Large areas of developed HSQ proved to be ion resistant, but critical problems appeared on the edges. In Figure 3.5, a scanning electron microscopy (SEM) image revealed that the edges of the mask are significantly weaker as they are sputtered away during the etching, despite re-exposing the resist with a dose of  $20000 \mu\text{C}/\text{cm}^2$ . So far, this effect has not been reduced and it is subject to further research.

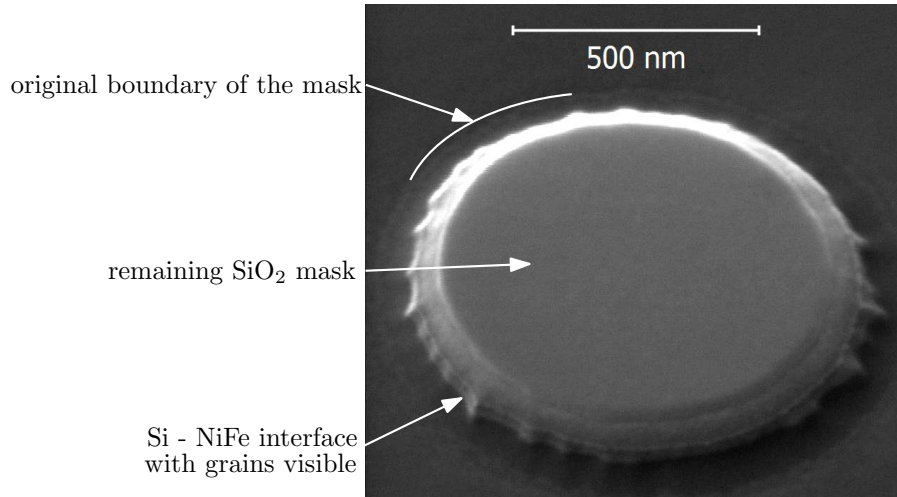


Figure 3.5: SEM image demonstrating the difficulties with ion beam etching using an HSQ mask. The edges of the mask were significantly weaker, therefore etched away before finishing of the process, leaving smaller patterns than intended with rough edges. Sample tilted to  $45^\circ$ .

For the IBE process, it is favorable to use negative-tone resists because a smaller area of the substrate needs to be exposed. But there are also positive-tone resists suitable for IBE, such as AR-P 6200<sup>4</sup>, if the lithography requirements allow it.

<sup>4</sup>Manufactured by ALLRESIST, <http://www.allresist.com>.

### 3.2.2 Metal mask by positive lithography and lift-off

When a suitable resist is not available, we can simply prepare a metal mask with a standard, positive-tone lithography process with lift-off. This process is schematically shown in Figure 3.6 and usually consists of more steps than the previous resist mask procedure. Titanium is often used because of its availability and slower etching rates comparing to other metals. The removal of the remaining mask is the main problem. Chemicals that dissolve one kind of metal also usually react with many other metals and it is often impossible to find a suitable chemical remover. This would not be a problem for applications where a thin layer of metal on top of the patterns is no issue. But for our purposes, it is not applicable because it would highly influence all electrical, optical and magnetic force measurements. Some of the commercial apparatus have secondary ion mass spectrometer (SIMS), which is very sensitive to the surface and permits a halt in the process right when the mask is removed leaving only an insignificant residue. The mask may have some defects on edges due to the lift-off process; this is usually solved by tilting the sample with respect to the ion beam and rotating it, where the edges are etched faster.

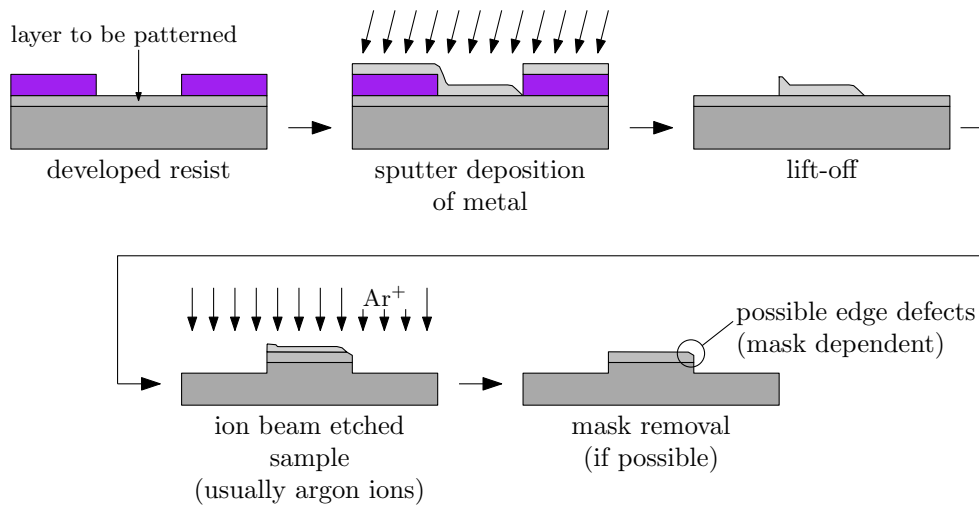


Figure 3.6: Schematics of the ion beam etching process using a metal mask. The mask is prepared by the lift-off process. The patterned layer is sputtered away and the remaining mask can be chemically removed or the process can be stopped precisely when the mask is sputtered away completely.

When an advanced IBE system is not available, aluminum can also be used as an etching mask. Its resistance to ions is lower, therefore a thicker mask is necessary. After finishing the process, the aluminium can be removed with TMAH, which is not too aggressive to many other metals [79]. TMAH also etches silicon, so substrates with a layer of  $\text{SiO}_2$  are the most suitable.

Despite the limited availability of aluminum in our sputtering system, we managed to try this process with unsatisfying results. The problem stemmed from a very low quality mask. SEM inspection (Figure 3.7) revealed low adhesion of aluminum on the substrates and also large grains, not allowing to complete the process in the expected quality.

The used apparatus was also a limitation for all IBE processes, as it possesses only a basic function, without features like sample rotation or SIMS. However a new dedicated IBE instrument will soon be installed in the Core Facilities of Central European Institute of Technology (CEITEC), giving this method a good future outlook.

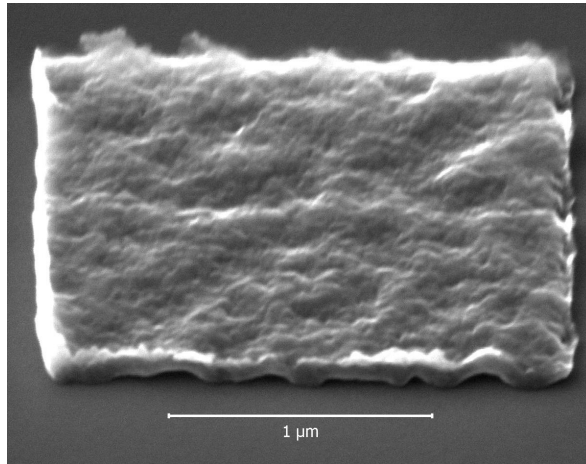


Figure 3.7: SEM image of an aluminium mask adhesion problem on a silicon substrate. Sample tilted to 45°.

### 3.3 Ion lithography by focused ion beam

Another way to achieve the ion beam etching is through direct milling using a focused ion beam (FIB). In this process, no mask is needed because the patterns are created by controlling the ion direction by deflection electrodes, not unlike in a scanning electron microscope (SEM). Focused ion beams columns are manufactured by several companies and they are usually installed into SEM systems, where they form a dual beam devices (schematically illustrated in Figure 3.8). When the sample is in the intersection of the two beams, it can be observed by SEM while it is being milled (or perhaps modified) by the focused ion beam. This provides good lithographic capabilities, as the spot size of a typical focused ion beam is less than 10 nm.

Our requirement is mostly to pattern a layer of Permalloy ( $\text{Ni}_{80}\text{Fe}_{20}$ ) that was previously sputtered onto a silicon substrate or to trim the edges of previously prepared patterns by lift-off as it is schematically shown in Figure 3.9. This can be done by fast scanning a rectangular write field with the focused ion beam, while the beam is blanked when it crosses the patterns to be left on the substrates. Sputtered films usually make polycrystalline layers with grain sizes in orders of tens of nanometres. As the ion beam milling is crystal orientation dependent [80], the grain boundaries are often revealed and residues of the layer are hard to be removed. In order to achieve a clean surface, the sample has to be over-etched into the substrate, which forms a large step that might be undesirable.

Another strategy is to remove the layer in a slow single (or double) scan (often called polishing scan), where the material is removed line by line and the crystal orientations do

not play as much of a significant role. The last useful strategy is to prepare the patterns by lift-off and simply cut off  $\sim 100$  nm of the edges to remove the unwanted defects.

While this tool can be very versatile, it is also slow and inapplicable for large series of samples. In Figure 3.10, a comparison of different approaches is demonstrated.

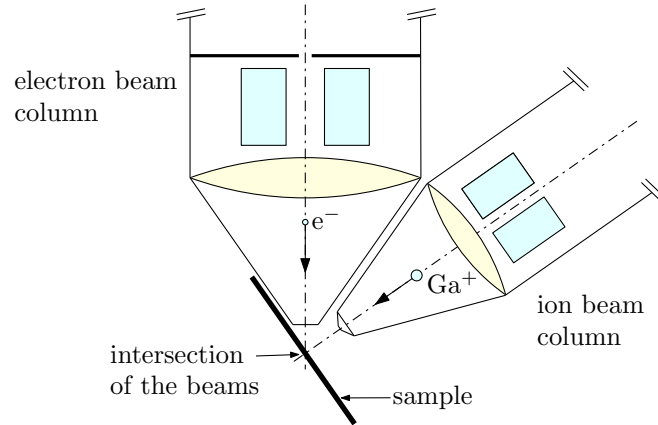


Figure 3.8: Schematics of TESCAN Lyra3 system combining a scanning electron microscope with a focused ion beam. The sample is usually tilted (the sample normal is parallel to the FIB's optical axis) and inserted into the intersection of the optical axes.

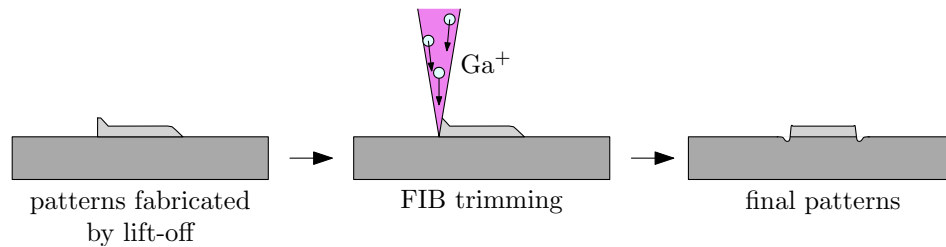


Figure 3.9: Schematics of the FIB trimming process. Patterns are previously prepared by lift-off and FIB is then used to trim the edges to achieve even edges.

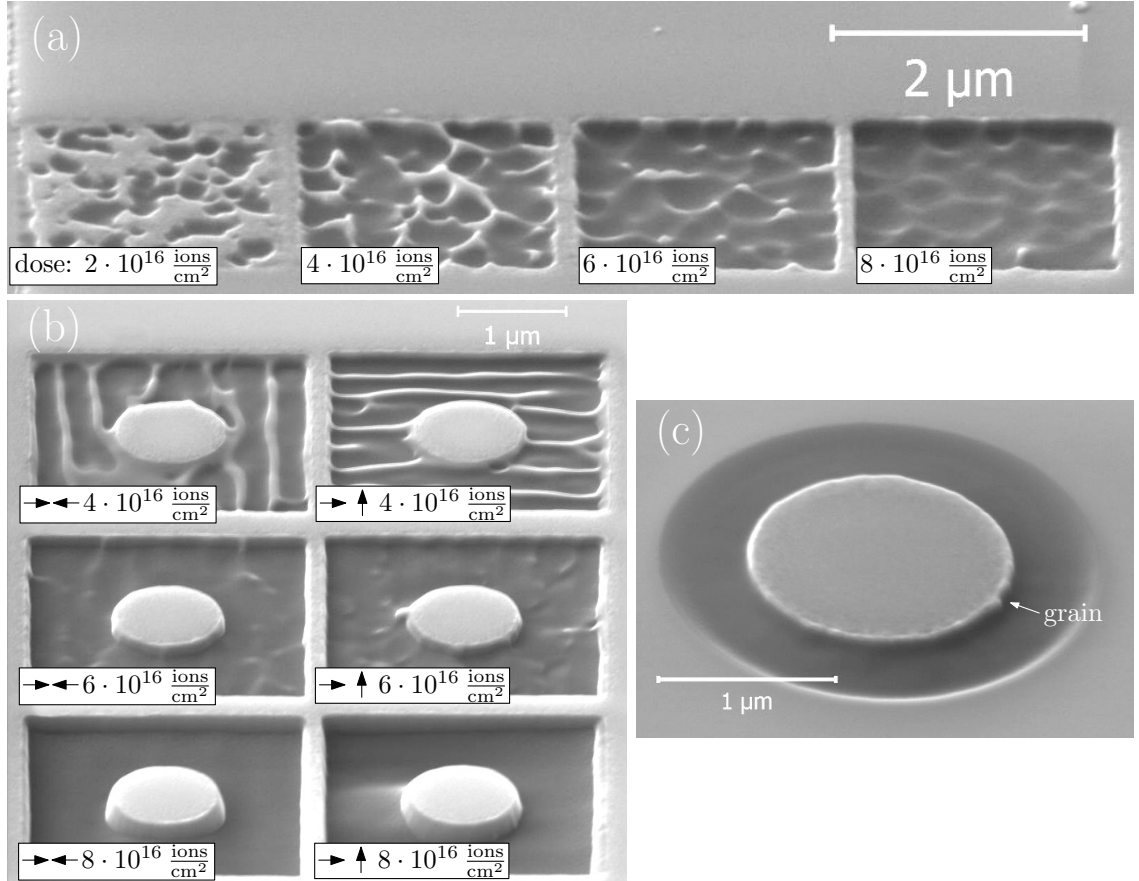


Figure 3.10: SEM images demonstrating the focused ion beam milling process. **(a)** Demonstration of the dose-dependence during the milling of a polycrystalline layer of Permalloy. A small dose invades the layer and reveals the individual grains. Increasing of the dose removes most of the layer, but to achieve the complete removal, the sample must be milled deep into the substrate (few multiples of the layer thickness). **(b)** Demonstration of different doses using two scan milling strategies. The dose increases from top to bottom: the left column shows strategy using two horizontal scans, the right column uses one horizontal and one vertical scan (indicated by the arrows). Increasing dose and change of the scanning direction bring different results. **(c)** A Permalloy disk cut out from a larger disk showing the best achievable quality of the edge.



### 3.4 Wet chemical etching

The other possible method of fabricating magnetic disks is wet chemical etching. This process would require lithographic preparation of an etching mask, after which the sample may be soaked into an liquid etchant. The mask can be stripped as the process is finished, resulting in a patterned layer on a substrate.

Our requirement is to preserve the patterned layer from oxidizing and/or corrosion, which excludes a large variety of chemicals (acids) from being used. This kind of process has never been used in our institute due to the unavailability of a suitable etchant and is thus a subject for further consideration.

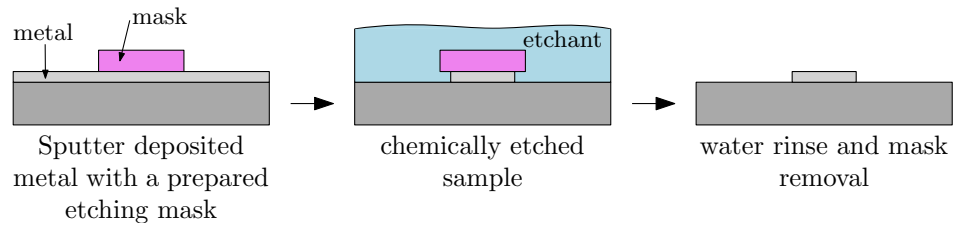


Figure 3.11: Schematics of the wet chemical etching process. The etchant usually underetches the mask, leaving smaller patterns than the mask.

## Chapter 4

# Characterization methods

This chapter describes the experimental methods used for characterization of magnetic vortices, mostly for measuring the vortex circulation. The main experiment in this work is the repeated measurement of the spin circulation after nucleation in a single magnetic disk. In order to measure the randomness of the process, we need a sufficiently large set of data of a single disk. So far, the only statistics found in literature was measured on arrays of elements (for example [49, 53]). Densely packed arrays may only have a pseudo-random distribution of circulations due to the magnetostatic coupling between the elements and may also be influenced by geometrical imperfections of different array elements. Thus the single-disk measurements have prior significance.

The main method used in this work is the measurement of **anisotropic magnetoresistance** (AMR). This method requires specific electric connections on the sample, having larger lithographic requirements, mostly available only in dedicated e-beam lithography systems. But when the sample preparation is mastered, the experiments are easily automated and can run non-stop without the presence of an operator giving it the significant capability of providing statistics.

From the point of resolution, **magnetic force microscopy** (MFM) is the best available method, as it uses AFM probes with magnetic coating. It can sense stray fields around magnetic structures which is particularly useful for sensing the vortex core polarity. Sensing the spin circulation requires a certain trick, as there are no stray fields around a vortex (due to the closed magnetic flux), except for those produced by the vortex core. We either have to place the sample into a magnetic field and measure the positions of the displaced cores or we can fabricate small cuts into the disks, breaking the flux closure and revealing the vortex circulation.

**Magneto-optical Kerr effect** (MOKE) measurements may be very versatile, but the diffraction limit of light at the visible spectra (in our case  $\lambda = 632.8\text{ nm}$  of He-Ne laser) is the restraining factor. Therefore it does not allow probing the vortex structure of  $\sim 1\text{ }\mu\text{m}$  disks, but it can measure other useful characteristics, for example hysteresis loops of a whole disk.

All of the mentioned techniques are used in the static regime, because the measurement times are very long compared to the characteristic timescale of the magnetization processes. The methods capable of providing fully time-resolved experiments are mainly the X-ray magnetic circular dichroism (XMCD) [8, 9, 67] usually performed in synchrotron facilities or

MOKE in some specific configurations using a pulsed laser source [81]. However the time resolved experiments are not necessary for this project. In the following sections, a closer description will be given to each of the used methods.

## 4.1 Anisotropic magnetoresistance

Magnetic samples exhibit a change of resistivity as a function of the angle  $\varphi$  between the vector of current density  $\vec{j}$  and the vector of magnetization  $\vec{M}$  [ $\varphi = \angle(\vec{j}, \vec{M})$ ]. If we suppose resistance  $\varrho_{\parallel}$  for  $\varphi = 0^\circ$  and  $\varrho_{\perp}$  for  $\varphi = 90^\circ$ , it can be shown, that the resistivity depends on  $\varphi$  as the following function [77]:

$$\varrho(\varphi) = \varrho_{\perp} + (\varrho_{\parallel} - \varrho_{\perp}) \cos^2 \varphi. \quad (4.1)$$

The phenomena is schematically shown in Figure 4.1. The experimental resistivity values for Permalloy were previously determined in [77]:

$$\begin{aligned} \varrho_{\parallel} &= 7.50 \cdot 10^{-7} \Omega\text{m} \\ \varrho_{\perp} &= 7.40 \cdot 10^{-7} \Omega\text{m} \end{aligned} \quad (4.2)$$

We can also define magnetoresistance as a relative change of resistance with respect to the saturation value:

$$\text{Magnetoresistance} = \frac{R - R_{\text{sat}}}{R_{\text{sat}}} \cdot 100\% \quad (4.3)$$

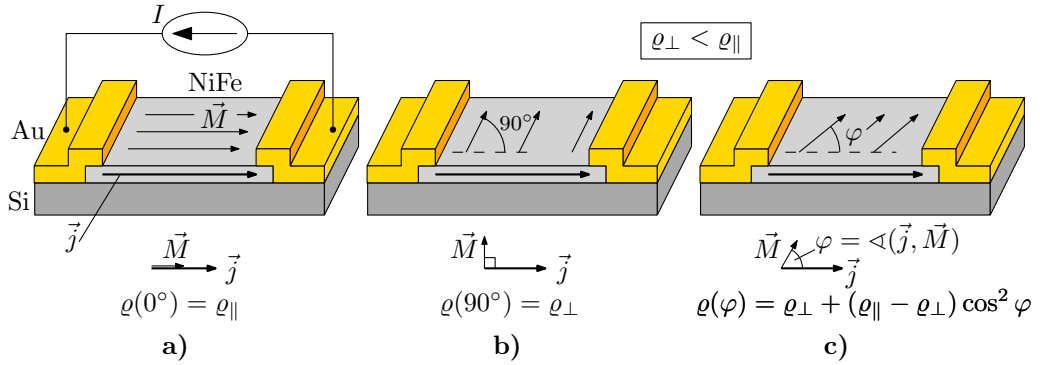


Figure 4.1: Principles of anisotropic magnetoresistance in a magnetic stripe. The resistivity of the layer varies with the angle  $\varphi$ , with it's maximum and minimum at  $0^\circ$  and  $90^\circ$  respectively.

### 4.1.1 Detection of the vortex circulation by anisotropic magnetoresistance

We can use AMR to detect the vortex circulation, if we place the electrodes on a disk and shift them to the side (Figure 4.2). This probes one half of the disk, while the other half of the disk has not as much influence on the measured resistance. When the disk is saturated, all magnetic moments are aligned in the  $y$  direction, giving the highest saturation resistance  $R_{\text{sat}}$ . Every other state has lower resistance, because there are also  $x$  components of magnetization present.

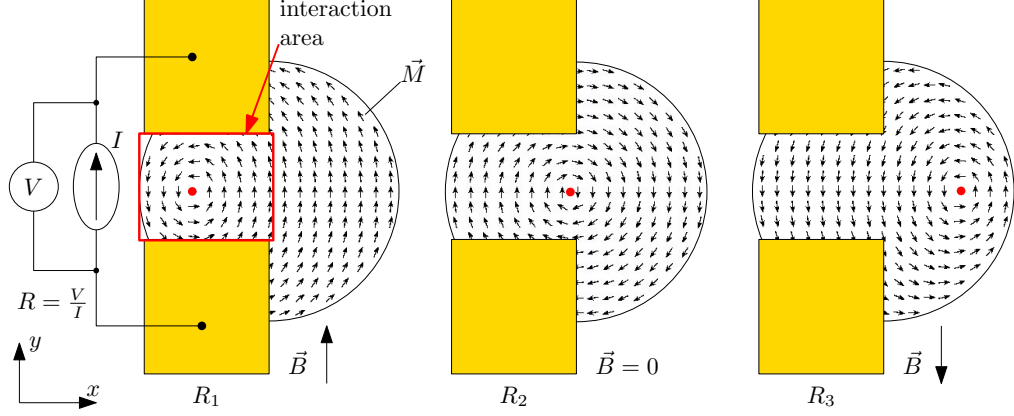


Figure 4.2: The detection arrangement is the most sensitive for the interaction area in between the Au electrodes (marked by the red rectangle). The measured resistance  $R$  changes with the state of the magnetization of the vortex. It decreases (increases), as the core is displaced inside (outside) of the electrodes by the external field  $\vec{B}$ . The saturated disk has the highest measurable resistance  $R_{\text{sat}}$  (image not shown). Based on the equation (4.1), we can deduce:  $R_1 < R_2 < R_3 < R_{\text{sat}}$ .

This two point AMR method was previously used to characterize  $4\text{ }\mu\text{m}$  Permalloy disks by X. Cui, et.al. [57] and it is significantly simpler than the four point method presented in [48, 55, 56]. The advantage comes with having smaller lithographic and interpretation requirements. The approach presented by X. Cui, et.al. consists of sweeping the magnetic field from saturation to saturation, while the opposite circulations are read based on a presence of a peak in the magnetoresistance curve as shown in Figure 4.3. This is in disagreement with our knowledge, as the presence of a peak only indicates the vortex nucleation through an  $S$ -state, while the vortex nucleates directly from saturation, there should be no peak present. The vortex circulation determination method that we propose consists of sweeping the magnetic field around the zero value, where the vortex core is displaced either towards the contacts or away from as shown in Figure 4.2. The core displacement results either into a drop or a rise of the measured resistance which allows us to deduce the vortex circulation based on the slope in resistance at the zero field. Additionally, the magnetoresistance curves exhibit a minimum when the vortex core is displaced approximately to the middle of the shifted contact pads and the position of the minimum is either in positive or in negative field in dependence on the vortex circulation.

To support the approach of shifted contact pads, a calculation of current density was carried out using COMSOL Multiphysics finite element solver giving the results of inhomogeneous current density distribution as shown in Figure 4.5. For the electrodes covering half of the disk in the  $x$  direction, it was calculated that 67.4% of the total current  $I_{\text{tot}}$  passes directly between the electrodes and 90% of the current passes roughly through  $3/4$  of the disk diameter giving a qualitative overview of the detection area.

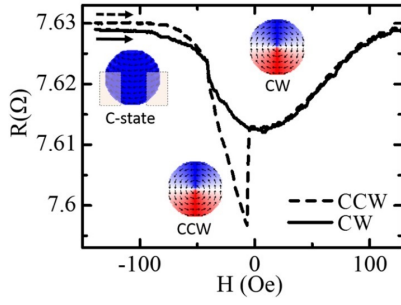


Figure 4.3: Representative magnetoresistance curves measured on 4  $\mu\text{m}$  disks by X. Cui et al. The circulation is distinguished based on the presence of the peak in the magnetoresistance curve (taken from [57]).

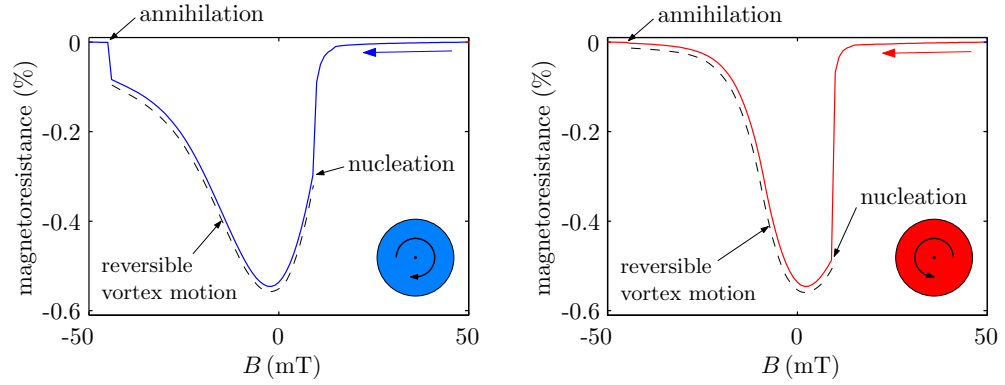


Figure 4.4: Example of AMR curves for each vortex circulation. Example of the AMR curves for opposite vortex circulations given by the opposite slope at  $B = 0 \text{ mT}$ . After the nucleation of a vortex state, the curve follows the reversible vortex motion until it is annihilated. The annihilation step is very different, because the change is much higher when the core is annihilated between the electrodes. Calculations neglect the influence of the disk outside of the contacts, which is the reason why the difference in the step is lower in real systems.

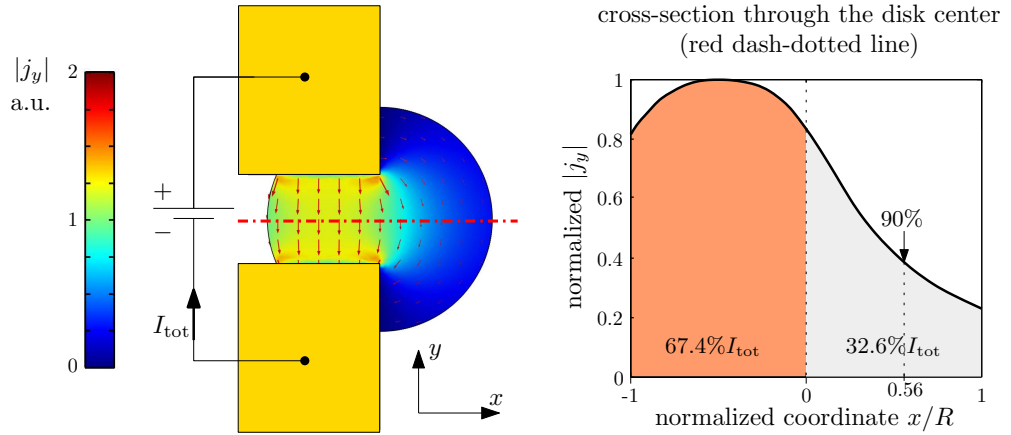


Figure 4.5: Calculated current density distribution in a Permalloy disk using COMSOL Multiphysics finite element solver. The electrodes (gold color) are assumed to be equipotential. Most of the current passes through the area between the electrodes, therefore the detection should be the most sensitive for the same area. The graph on the right side shows the dependence of normalized current density  $|j_y|$  along the cross-section through the disk center (marked by the red dash-dotted line).

#### 4.1.2 Experimental setup

Figure 4.6 shows the schematics of the used AMR experimental setup. The sample was inserted between the yokes of an electromagnet powered by the bipolar current source Kepco BOP 20-5M (20 V and 5 A limits). The magnetic field was calibrated using the teslameter F.W. Bell 6010.

The resistance measurement requires a very sensitive technique, because the changes are very small, in order of  $10^{-3} \Omega$ . We used Keithley 6221 current source and 2182A nanovoltmeter connected into the so-called DELTA mode – a method using alternating square wave current for effective filtering of noise with 10 nV voltage measurement sensitivity, even declared to outperform lock-in amplifiers [82]. The probe current 100-500  $\mu\text{A}$  was sufficient for measuring  $\sim 20 \Omega$  resistances with precision of about  $10^{-4} \Omega$ .

The experiment was controlled by a computer using National Instruments LabVIEW 2013 development environment; all connected devices were commanded using the general purpose interface bus IEEE-488 (GPIB). The sample was placed into the environmental furnace TIRA miniTTC 4006 to stabilize temperature drifts with the possibility of heating up to  $170^\circ\text{C}$  or cooling down to  $-40^\circ\text{C}$ .

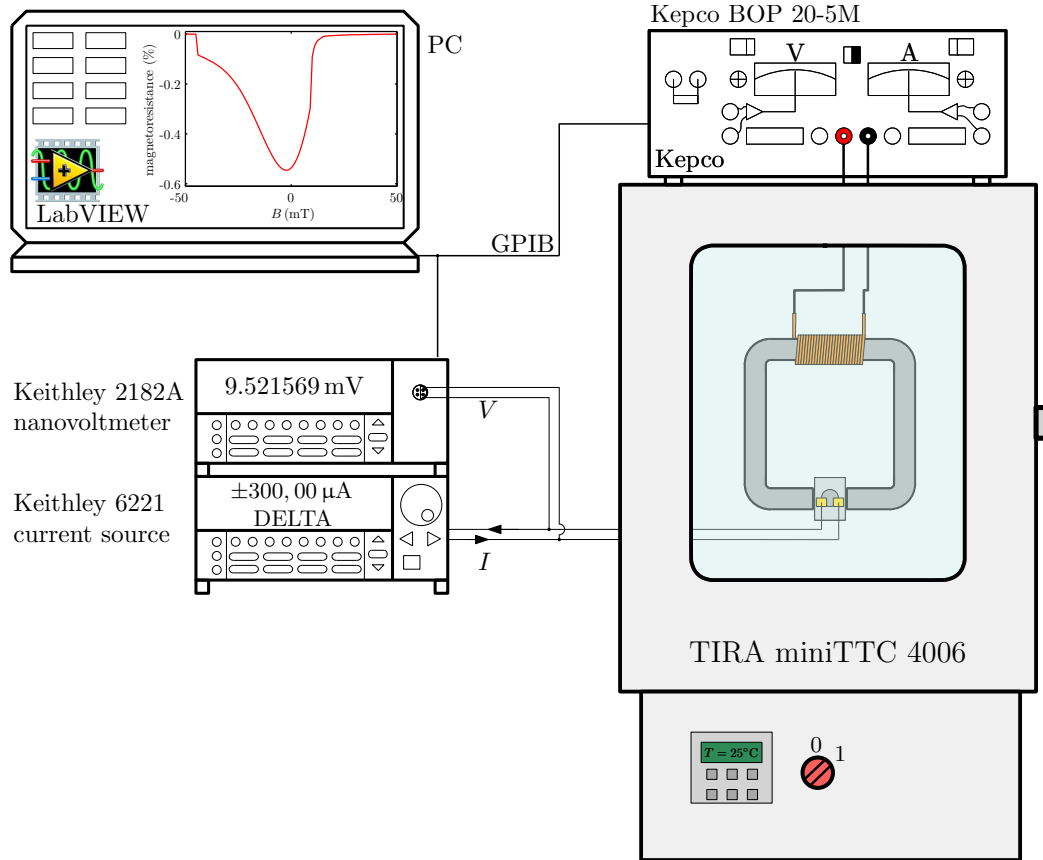


Figure 4.6: Schematics of the experimental setup. The sample and the electromagnet are placed into an environmental furnace to stabilize temperature. The instruments Kepco BOP 20-5M and Keithley 6221/2182A are connected to a computer via GPIB interface and the experiment is controlled with the developed LabVIEW program.

## 4.2 Magnetic force microscopy

Magnetic force microscopy (MFM) is based on one of the most common scanning probe microscopy (SPM) methods called atomic force microscopy (AFM). It uses a sharp silicon tip (apex radius usually  $<10\text{ nm}$ ) mounted on a cantilever that is built on a larger chip. The basic principle is shown in Figure 4.7(a): the probe scans along the surface, where the atomic forces cause the tip to deflect vertically, which is usually detected optically by a laser beam reflection from the cantilever towards a four-quadrant photodiode. The deflections may be very small, but subnanometre measurement precision is usually achieved.

In the last decades, AFM using silicon probes became a standard method for high resolution 3D imaging of a sample surface as well as it brought a variety of derived methods. MFM is now one of the standard methods for imaging magnetic nanostructures. It uses non-contact AFM probes with magnetic coating to sense the stray fields created around magnetic structures. Besides specialized probes, the MFM microscope operates using the so-called “lift mode” technique, where the probe passes twice for every scan line as shown in Figure 4.7(b). The first scan mainly provides the topography, while the second scan is performed at an elevated height (parameter called lift-height, approximately  $20\text{ nm}$  from the topography scan) where the electromagnetic forces dominate.

Commercial probes are mostly CoCr coated, but other magnetic materials are applicable as well. On the basis of works [13, 84] we use the Olympus AC240TS probes [Figure 4.7(c)]

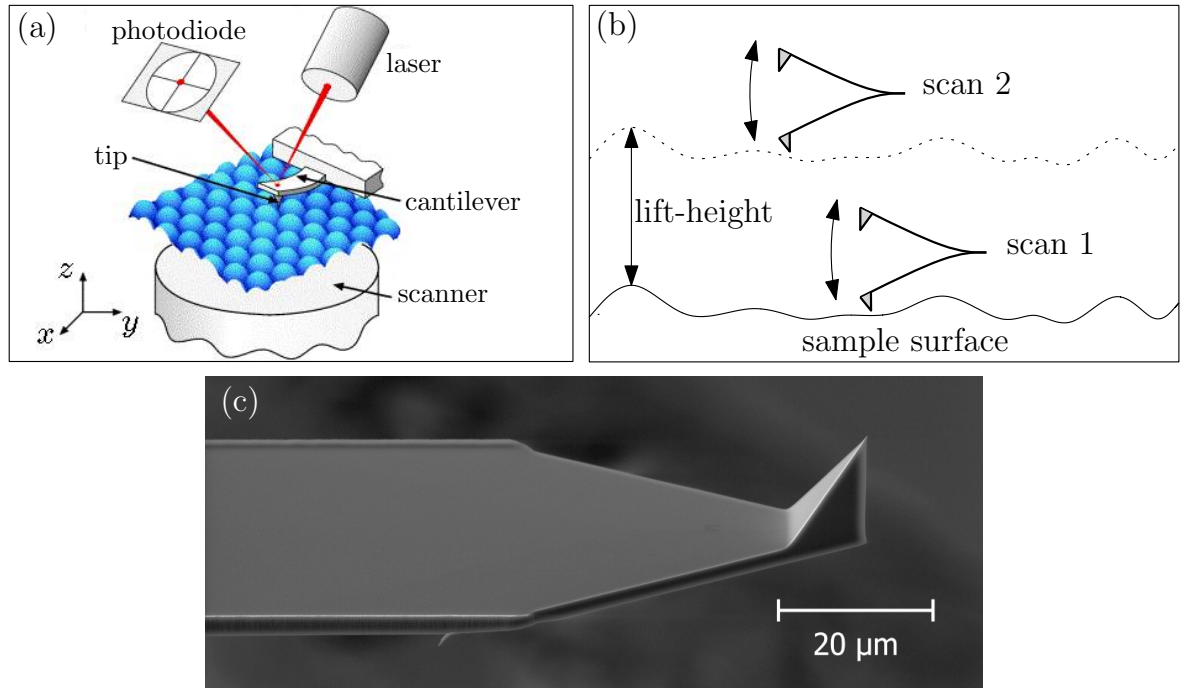


Figure 4.7: (a) Basic principle of AFM. The cantilever tip scans the sample surface, while deflection is detected using a laser reflection into a photodiode (taken from [83]). (b) Two-pass technique called lift mode utilized in MFM. The topography is measured in the first scan, then probe is elevated for the second scan, where the electromagnetic forces are dominating. Adapted from [84]. (c) SEM image of the used cantilever Olympus AC240TS.

with home-made coating (Permalloy or cobalt coating). Permalloy coated probes proved to have a very good capability of vortex core imaging because they carry a lower magnetic moment which causes less disturbances in the measured nanostructure. On the other hand, Permalloy coating is easily re-magnetized which forbids measurements in an external field. Cobalt coated tips are harder to be re-magnetized which makes them capable of measurements in external magnetic field, typically for imaging of the displaced vortex cores.

### 4.3 Magneto-optical Kerr effect

Magnetic properties of nanostructures may be measured optically, using the magneto-optical Kerr effect (MOKE). There are three possible configurations of the measurement: polar, longitudinal and transversal as it is demonstrated in Figure 4.8. The polar and longitudinal Kerr effects are characterized by a complex angle  $\Phi = \theta + i\epsilon$  of the plane of polarization of linearly polarized incident light upon reflection from the surface of a ferromagnetic material [85]. The real part of the complex angle is the Kerr rotation  $\theta$  and the imaginary part is the Kerr ellipticity  $\epsilon$ . It may be shown, that both Kerr rotation and ellipticity are linearly proportional to the dot product  $\vec{k} \cdot \vec{M}$  where  $\vec{k}$  is the wave vector of the incident light and  $\vec{M}$  is the magnetization vector [86]. The transversal Kerr effect has a different physical origin than the polar and longitudinal configurations; it does not affect polarization but reflectivity.

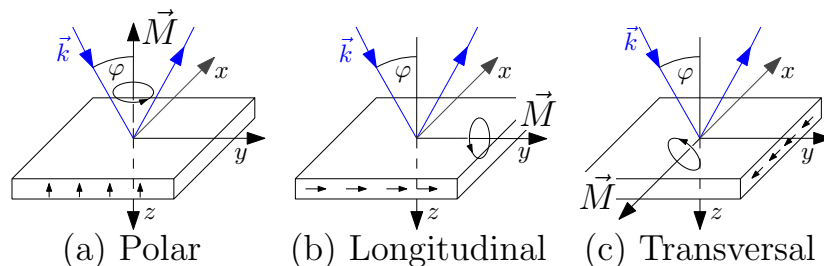


Figure 4.8: Three possible configurations of magneto-optical Kerr effect measurement (taken from [86]).

Our instrument at IPE BUT is under the development led by L. Flajšman and the detailed description is given [86, 87]. It uses a microscope objective to focus a He-Ne laser into a 500 nm spot and is equipped with piezo-elements to provide the scanning capability (20  $\mu\text{m}$  scan size). The sensitivity to achieve a desired magnetization direction is chosen by precise positioning of the laser beam on the entrance pupil of the objective. The sample is placed into an electromagnet powered by a bipolar current source. When an alternating magnetic field is needed, a waveform generator controls the current source through the analog input. The detector consists of a Wollaston prism (polarizing beam splitter) and two photodiodes for each of the beams coming out from the prism. The differential signal is read by a data acquisition card from a home made board connected to the photodiodes. The whole apparatus is computer controlled using National Instruments LabVIEW development system (manipulator, detector, magnet). Besides measurements of local hysteresis loops within the optical spot, the instrument may also be used as a scanning Kerr microscope.



# Chapter 5

## Results

This chapter presents the achieved results that consist of three parts:

1. simulations of anisotropic magnetoresistance,
2. measurements of the vortex circulation by anisotropic magnetoresistance on single disks and pairs of disks,
3. supporting measurements using magnetic force microscopy and magneto-optical Kerr effect.

The simulations were carried out in order to correctly interpret the anisotropic magnetoresistance curves of a single magnetic disk. Then, repeated magnetoresistance measurements of micrometer-sized Permalloy disks were performed to study the nucleation randomness of a single disk and to inspect the magnetostatic coupling in pairs of disks. In the end of this chapter, complementary magnetic force microscopy measurements are also presented. Magneto-optical Kerr effect measurements proving the existence of  $S$ -states are shown as well.

### 5.1 Simulations of anisotropic magnetoresistance

Magnetoresistance curves were calculated by a home-made code using the simulation outputs from Object Oriented Micromagnetic Framework (OOMMF) on a  $1\text{ }\mu\text{m}$  disk with the cell size  $(3.5 \times 3.5 \times 20)\text{ nm}$ . Three simulations numbered 1-3 were used; the corresponding hysteresis loops are shown in Figure 5.1 also with the magnetization images of several points of interest along the loops. The most important differences are the nucleation fields of -9, 0 and 9 mT for Simulations 1-3 respectively. The vortex nucleation mechanism is triggered by thermal fluctuations, however Simulations are carried out at the temperature of 0 K, which causes the vortex to nucleate later than in reality. Simulations 1 and 2 were used as they came out from OOMMF, while Simulation 3 was obtained from Simulation 1 by moving the core backwards after nucleation and replacing the original points. This can substitute the thermally induced nucleation trigger in real samples when we need to obtain a positive nucleation field; the vortex core motion is reversible which justifies this approach. The measured disks were almost always larger than  $1\text{ }\mu\text{m}$ , but no larger disks were calculated because the computation time would be very long ( $\sim$ weeks). Nonetheless the main difference between the disks with varying sizes are the nucleation and annihilation fields, while the shape of the the hysteresis

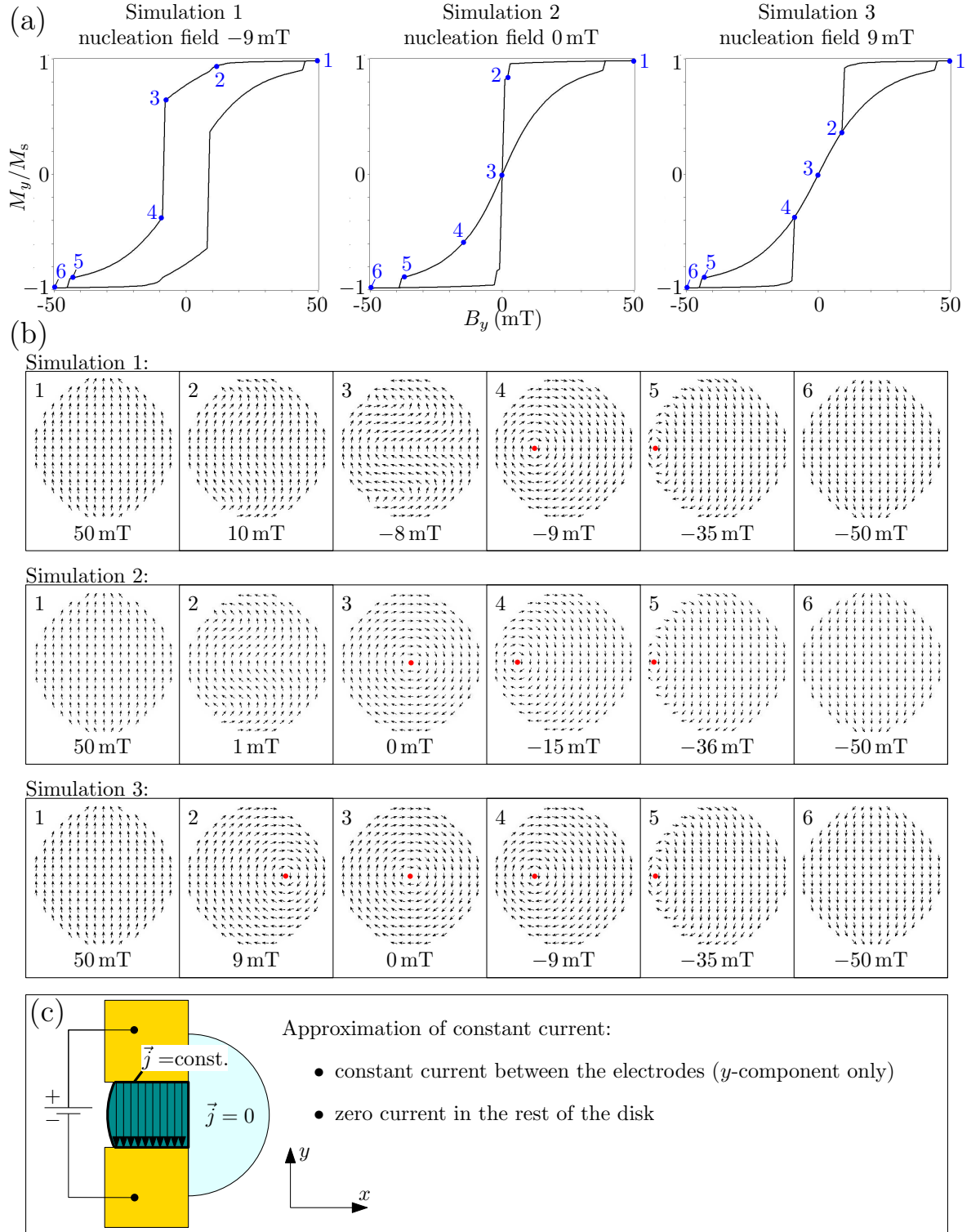


Figure 5.1: (a) Hysteresis loops of the OOMMF micromagnetic simulations for  $1\ \mu\text{m}$  disks with nucleation fields  $-9$ ,  $0$  and  $9$  mT. (b) Images of magnetization in points of interest. (c) Schematic illustration of the approximation used in calculations.

loops remains similar, allowing us to qualitatively compare simulations and measurements carried out on disks with different sizes only by scaling the  $B$  axis.

To simplify the calculations, the approximation of constant current between the electrodes and zero current elsewhere was used [schematically shown in Figure 5.1(c)]. Then the problem reduces to calculating the resistance of each cell by the equation (4.1) and to connecting the cells into parallels and series of resistors.

The calculation results are shown in Figure 5.2. The curves for contacts covering the whole disk in the  $x$  direction (top graph) are identical for both circulations due to the symmetry of the problem. The magnetization configuration is also assigned for several points of interest to clarify the corresponding resistance and the magnetization state. The rest of the calculation results show curves for both circulations and four sizes of the contacts (covering  $\frac{3}{10}$ ,  $\frac{1}{2}$ ,  $\frac{7}{10}$  of the disk or the whole disk). The  $y$ -axis is given as the percentual magnetoresistance defined by equation (4.3) to obtain comparable scales, because different contact layouts have different resistances.

From the magnetoresistance curve calculated from Simulation 1, it is apparent that the sharp peak (clearly visible for larger contacts) is connected with the presence of an  $S$ -state in the disk prior to the nucleation of the vortex core [point 3 of Simulation 1 in Figure 5.1(b)]. In the  $S$ -state, there is a large  $M_x$  component of magnetization (transversal to the current density  $\vec{j}$ ) between the contacts resulting in the low resistance value. On the other hand, the vortex state in Simulation 3 nucleated directly from a  $C$ -state and the peak does not appear in the calculated curves. This explanation of the magnetoresistance curve shape opposes the concept introduced by X. Cui et al. in [57] where they detect a sense of circulation from the presence of a peak in magnetoresistance curves. According to our simulation and also to the experimental findings [see Section 5.2 and Figure 5.5], the presence of the peak simply indicates the vortex nucleation through an  $S$ -state. We propose a different concept, where the circulation readout is based on the slope of the magnetoresistance at the zero field, which is based on the vortex core moving either towards the contacts or away from them, and thus shows the sense of the circulation inside the disk.

One important difference for clockwise and counter-clockwise circulations is the annihilation step, that is very high for the annihilation taking place between the contacts and low for the annihilation taking place outside of the contacts. The step difference (for opposite circulations) in real systems proved to be smaller than the simulated value. The vanishing step for the counter-clockwise circulation may be explained by the used approximation of zero current outside of the contacts. The annihilation is detected in real systems, because there is presence of a non-zero current also outside of the contacts.

Figure 5.3 shows the calculated minor loops of a  $1\text{ }\mu\text{m}$  disk for the field range from  $-9\text{ mT}$  to  $9\text{ mT}$ . This demonstrates that the slope at the zero field is opposite for opposite vortex circulations. This feature is used for automated detection of the sense of the spin circulation in magnetic disks. The slope is the highest for the configuration when the contacts are covering half of the disk. The resistance also has a minimum when the vortex core is approximately in the middle of the contact pads. The position of the minimum changes the sign with respect to the vortex circulation.

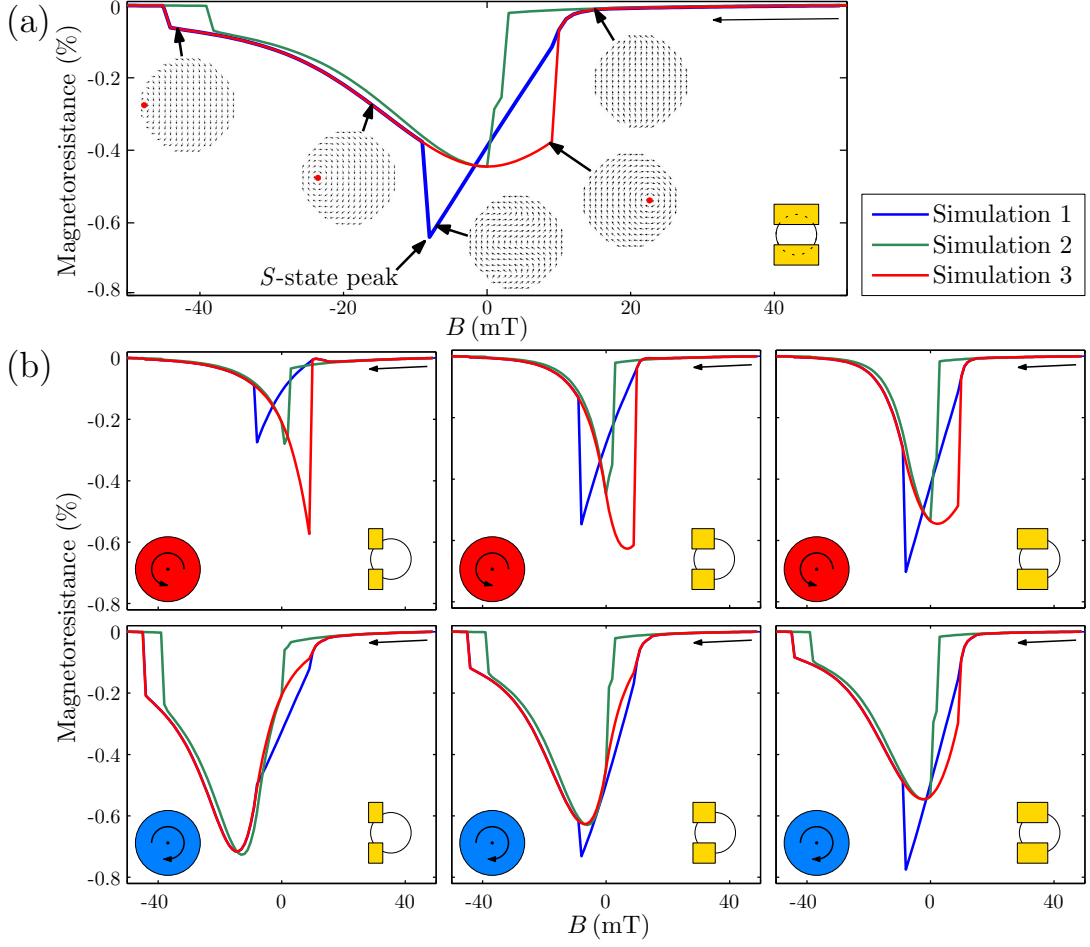


Figure 5.2: Calculated magnetoresistance curves using three simulation outputs from OOMMF. The calculations were carried out for four sizes of contacts, covering  $\frac{3}{10}$ ,  $\frac{1}{2}$ ,  $\frac{7}{10}$  of the disk or the whole disk. (a) When the contacts cover the whole disk, the curves are equal for both circulations. (b) The curves for smaller contacts are presented for counter-clockwise circulation in the middle row and for clockwise circulation in the bottom row.

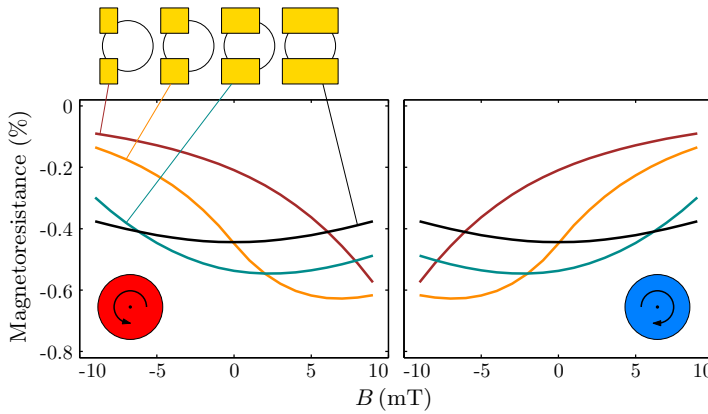


Figure 5.3: Calculated magnetoresistance curves of minor loops for the range from  $-9$  mT to  $9$  mT (vortex core is moving around the center position). When the contact covers the whole disk, the minor loop is symmetric around zero. For smaller contacts, there is an opposite slope at the zero field for opposite circulations which is essential for the used detection method.

## 5.2 Measurements of anisotropic magnetoresistance

Magnetoresistance measurements were carried out on disks with diameters ranging from 4  $\mu\text{m}$  down to 1  $\mu\text{m}$  and thicknesses ranging from 20 nm to 100 nm. All samples were prepared using two step e-beam lithography on silicon substrates with a 20 nm layer of thermal  $\text{SiO}_2$ . The sample preparation consisted of three main steps:

1. The disk was fabricated by e-beam lithography, ion beam sputtering and one of the methods described in detail in Chapter 3 (lift-off, IBE or FIB trimming). The process consisted of the following steps:
  - The substrates were cleaned in acetone and isopropyl alcohol (IPA) baths using an ultrasonic cleaner for 1 minute each.
  - A 500 nm resist layer was spin-coated at 3500 RPM for 30 s onto the substrates using a 495K PMMA resist of 5.5% concentration in anisole and spin-coater Laurell WS-400-6NPP.
  - The resist was exposed with a  $400 \mu\text{C}/\text{cm}^2$  dose of electrons at 30 keV energy using TESCAN Lyra3 FIB-SEM.
  - The exposed resist was developed for 1 minute in methyl isobutyl ketone (MIBK) and isopropyl alcohol (IPA) of 1:3 ratio.
  - A layer of Permalloy was deposited using Kaufman ion beam sputtering apparatus with base pressure of  $5 \cdot 10^{-5}$  Pa, working argon pressure of  $2 \cdot 10^{-3}$  Pa and sputtering rate of  $1.2 \text{ \AA}/\text{s}$  for Permalloy.
  - The resist layer was dissolved in acetone and the residues were removed using the ultrasonic cleaner. The substrates were then blow-dried with nitrogen.
  - The edges of the prepared patterns were FIB trimmed using TESCAN Lyra3 FIB-SEM (optional).
2. The contact pads were placed onto the disk using a second e-beam lithography step (the same procedure as in the previous point), while a 100 nm thick layer of gold was deposited instead of Permalloy with the sputtering rate of  $2.4 \text{ \AA}/\text{s}$ . An alignment procedure was used in order to match the write fields of the two steps, so the contact pads would be correctly placed on the disk (approx. 100 nm placement error for the used instrument).
3. The silicon substrates were glued into packages compatible with the DIP8<sup>1</sup> socket which was used in the sample holder for fixation in the electromagnet (shown in Figure 5.4). The contact pads prepared in the second step were wirebonded to the package to establish the electrical connections to the sample holder (ultrasonic wire bonder TPT HB16).

---

<sup>1</sup>Dual in-line package (8 pins) is a standard electronic component package.

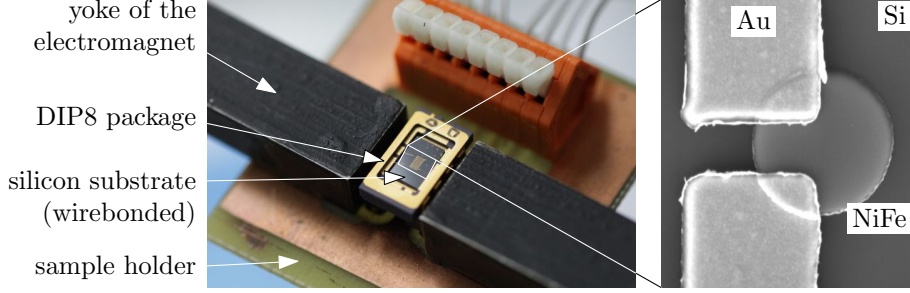


Figure 5.4: Photograph of the sample holder used for the magnetoresistance measurements with a SEM image of a typical contacted disk.

We also attempted to measure smaller disks, but  $1\text{ }\mu\text{m}$  disks were already very challenging to fabricate. The contacts were either not correctly placed or were interconnected between each other due to the proximity effect<sup>2</sup>. The finished samples were then measured in the experimental setup described in Subsection 4.1.2. We started with single disk measurements. The first set of samples was prepared by the lift-off process. The lift-off process is the least promising technique, because of its edge roughness, but it is especially useful while the second step is still being optimized; so the least time is lost when the contacts are not correctly placed on the disk. After the preparation of contacts was mastered, the other possibilities (ion beam etching and FIB trimming) were also tested. The following sections present the results obtained on single disks and on pairs of disks. The single disks were tested with the goal of achieving random nucleated vortex states. Pairs of disks were then tested to inspect the magnetostatic coupling.

### 5.2.1 Measurements on single disks: a pursuit of randomness

Table 5.1 shows the types samples prepared by all of the methods. The task of proving the randomness started on samples prepared by the lift-off method (explained in Section 3.1), because it is the easiest approach. We prepared more than one hundred samples of which approx. fifty were functional.

We measured the vortex circulation using anisotropic magnetoresistance measurements on disks with shifted contacts with the method described in Subsection 4.1.1. Two possible curve shapes occurred, either with or without a peak in the magnetoresistance curves. Based on our simulations presented in Section 5.1, we deduced that the vortex nucleates using two mechanisms:

- $C$ -state  $\rightarrow$  vortex, when there is no peak.
- $C$ -state  $\rightarrow S$ -state  $\rightarrow$  vortex, when there is a peak present in the magnetoresistance curve.

In the  $S$ -state, the resistance is low because there is a large  $M_x$  component of magnetization (transversal to the current density  $\vec{j}$ ). In general, nucleation through the  $S$ -state was more

<sup>2</sup>The proximity effect causes the resist outside of the scanned patterns to receive a non-zero dose and results in enlarging the patterns upon development. It is described for example in Section 2.4 of [73].

Table 5.1: Summary of prepared single disk samples.  $D$  and  $L$  are the disk diameter and thickness,  $N$  is the number of fabricated samples, func. says how many samples were functional (even when a significant noise was present) and rand. gives the number of samples exhibiting at least partial randomness.

<b>lift-off:</b>					<b>FIB trimming:</b>				
$D$ ( $\mu\text{m}$ )	$L$ (nm)	$N$	func.	rand.	$D$ ( $\mu\text{m}$ )	$L$ (nm)	$N$	func.	rand.
1	20-100	27	5	0	1.5	30-50	39	15	3
1.5	30-100	15	4	1	4	30	2	1	0
2	30-100	5	4	0	<b>Ion beam etching:</b>				
3	50	5	3	0	$D$ ( $\mu\text{m}$ )	$L$ (nm)	$N$	func.	rand.
4	30-50	35	18	1	4	30	20	1	0
total		87	34	2					

common in larger disks, while the smaller disks often nucleated without any magnetoresistance peak present, indicating nucleation through a  $C$ -state. Some samples exhibited both types of nucleation, through the  $C$ -state and the  $S$ -state. Representative magnetoresistance curves for a  $2\mu\text{m}$  and a  $4\mu\text{m}$  disks indicating both types of nucleation are shown in Figure 5.5. After the nucleation, the curves are identical when the nucleated state has the same circulation. This interpretation of the magnetoresistance curves is in contradiction with the work published by X. Cui et al. [57], where they presented a concept of the circulation read-out based on the presence of a peak in the measured magnetoresistance. Our concept of the circulation readout is based on the sign of the slope at the zero field, where the vortex core is moving either towards the contacts or away from them.

To further prove that the vortex may nucleate through an  $S$ -state, scanning Kerr microscopy measurement was performed showing a good agreement with simulations (see Section 5.4).

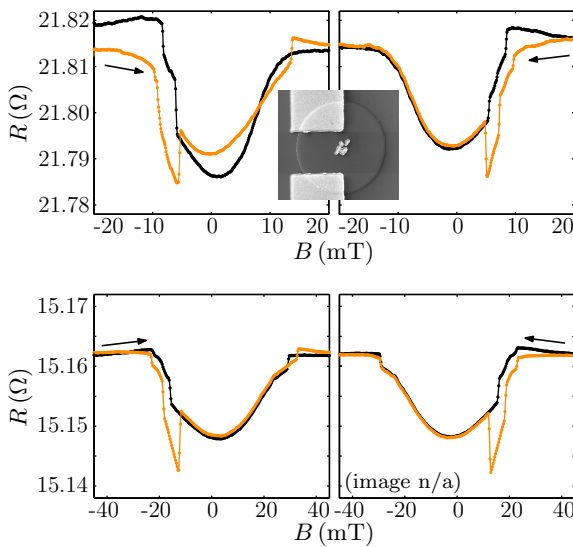


Figure 5.5: Representative anisotropic magnetoresistance measurements on a  $4\mu\text{m}$  disk (top) and a  $2\mu\text{m}$  disk (bottom). The presence of the peak (orange curves) may be interpreted that the vortex nucleates through an  $S$ -state, while the black curves indicate a nucleation through a  $C$ -state. The circulation may be read based on the slope at the zero field (or eventually by reading the position of the magnetoresistance minimum). The orange and black curves in the top left graph have opposite circulation, while they have identical circulations between each other in the other three graphs.

In the study of randomness, all of the samples prepared by the lift-off process did not

show any random behaviour with just two exceptions. One of the  $4\text{ }\mu\text{m}$  disks exhibited partial randomness, while the geometry observed in SEM was not significantly different from the other samples. The randomness was not measured on a larger statistic, because the sample broke down before a longer measurement. The other sample was a  $1.5\text{ }\mu\text{m}$  disk, where the asymmetry created due to the shadowing effect was placed on the bottom of the disk (the SEM image and representative magnetoresistance curves are shown in Figure 5.6). This could have established the randomness, since the system was still (left-right) symmetrical with respect to the magnetic field. A statistical sample of 75 000 measurements was obtained, where the disk was saturated and then a minor loop was acquired for each measurement. The acquisition time of a minor loop measurement is only 3 s compared to 1 min of the full curve measurement time. Figure 5.8(a) shows the statistical data, that resulted in the circulation distribution 79.4:20.6 % between counter-clockwise and clockwise circulations. This could be labelled as only partially random as most of the acquired measurements were counter-clockwise.

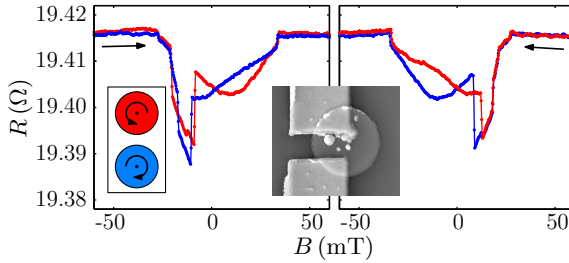


Figure 5.6: Anisotropic magnetoresistance curves of a  $1.5\text{ }\mu\text{m}$  disk (prepared by lift-off) that exhibited randomness [shown in Figure 5.8(a)]. Opposite circulations are denoted by red and blue colors, while they were evaluated based on the slope at the zero field.

The initial experience with the FIB trimming of the disk edges was rather disappointing, because all prepared samples exhibited a high resistance value in units of  $\text{k}\Omega$ . It was found, that the reason was the SEM contamination of the sample created during the imaging; a thin layer of carbon may be deposited during SEM observation. When the SEM imaging was avoided, the resistance was again on the normal level of approx.  $20\text{ }\Omega$ . After overcoming the initial difficulties, FIB trimming proved to be a promising method for well-defined edges of the prepared disks. Statistics were obtained for two similar samples, for which the magnetoresistance curves are shown in Figure 5.7 and the corresponding statistics are presented in Figure 5.8(b) and (c). After acquiring 89 000 measurements, the first sample had a similar circulation distribution like the previous sample prepared by lift-off. The second sample had the final distribution 66.5:33.5 % but the blue points of Figure 5.8(b) suggest that the randomness was changing during the measurement with no apparent explanation (the conditions remained the same). We tried to stabilize the randomness by increasing the temperature to the  $80^\circ\text{C}$  level which proved to equalize the probabilities of the two possible circulations leading to the final distribution 54.7:45.3 %. This is considered to be a very good result; on the other hand, some of the samples prepared by FIB trimming did not exhibit any randomness, while there was no significant difference in the SEM images.

Disks thicker than  $50\text{ nm}$  were not fabricated by FIB trimming because the grains grow larger in thicker layers prepared by sputtering. This prevents a good quality of the edges to be achieved. In layers thicker than  $30\text{ nm}$ , no significant improvement may be obtained comparing to the lift-off process.



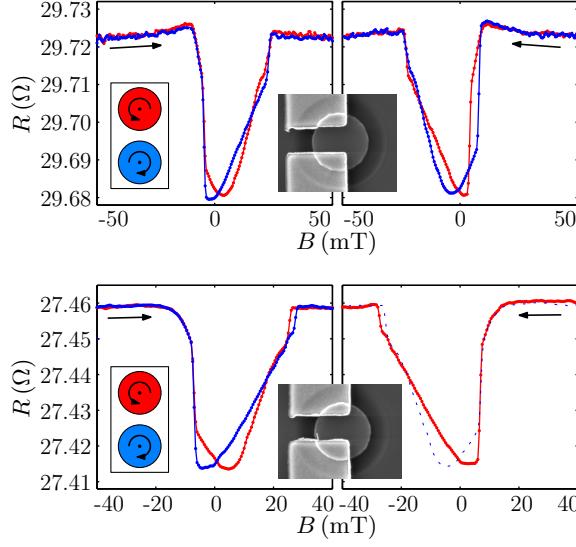


Figure 5.7: Anisotropic magnetoresistance curves of two similar  $1.5\text{ }\mu\text{m}$  disk prepared by FIB trimming. Both disks exhibited randomness [shown in Figure 5.8(b) and (c)], while the opposite circulations are denoted by red and blue colors. The dashed, blue curve in the bottom-right graph represents the expected magnetoresistance that did not occur during the initial measurement of full curves and before measuring only the minor loops to accelerate the measurement.

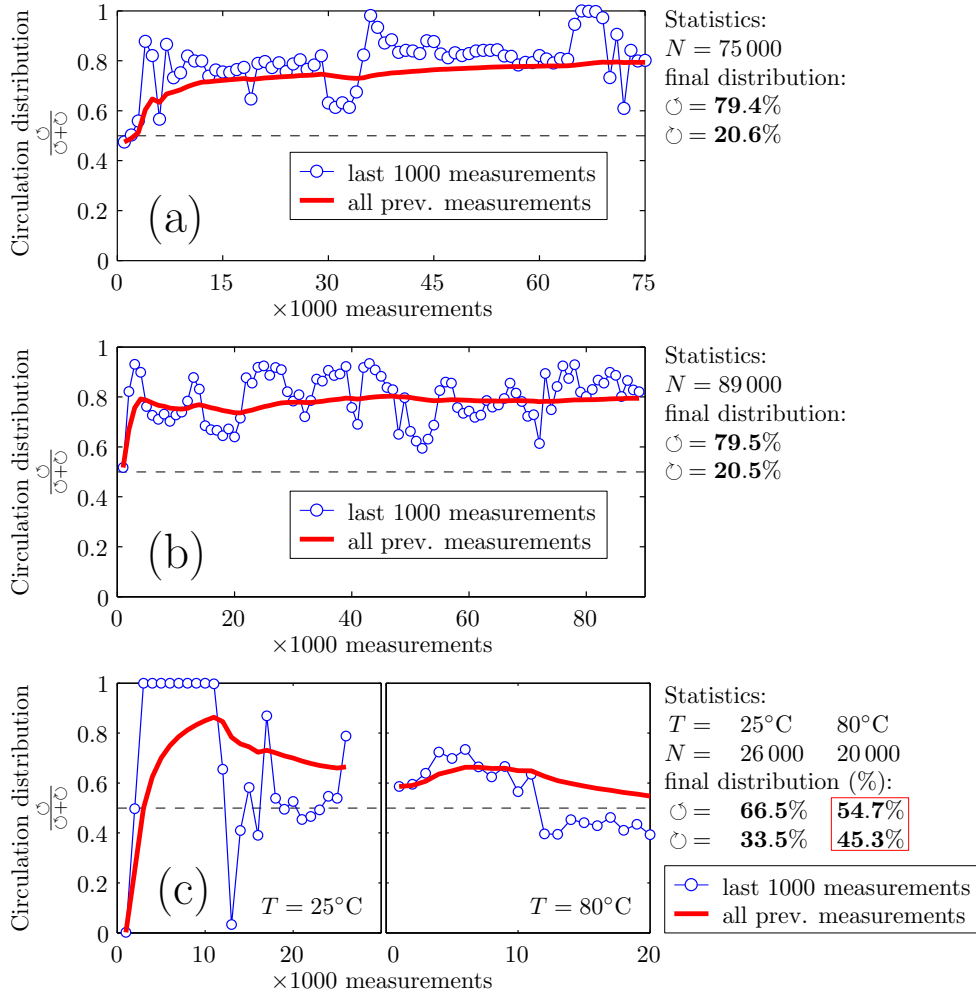


Figure 5.8: Results of the statistics measurements for three  $1.5\text{ }\mu\text{m}$  disks. (a): Disk prepared by lift off, the corresponding magnetoresistance curves may be found in Figure 5.6. (b-c): Disks prepared by FIB trimming, the corresponding magnetoresistance curves are shown in Figure 5.7. Best CCW-CW ratio was obtained in (c) when the sample was heated to  $80^\circ\text{C}$ .

### 5.2.2 Pairs of disks

Experiments on pairs of disks were carried out despite the presumption of randomness of single disks being only partially fulfilled. Pairs of disks were prepared by FIB trimming because it is the most promising fabrication method. The summary of prepared samples may be found in Table 5.2.

Table 5.2: Summary of prepared pairs of disks.  $D$  and  $L$  are the disk diameter and thickness,  $N$  is the number of fabricated samples, func. says how many samples were functional (even when a significant noise was present) and opposite  $c$  gives the number of samples exhibiting opposite circulations upon nucleation.

<b>FIB trimming:</b>				
$D$ ( $\mu\text{m}$ )	$L$ (nm)	$N$	func.	opposite $c$
4	30	3	2	0
1.5	30	25	6	2

Contacts were prepared on each of the disks, so both of them could be measured consequently. Two out of six functional samples with disks  $1.5\ \mu\text{m}$  in diameter exhibited opposite vortex circulations. The measured magnetoresistance curves are shown in Figures 5.9 and 5.10. This unfortunately does not prove the magnetostatic coupling, because the other 4 samples exhibited either the same circulations or some of them were even partially random. It is also expected, that the coupling would be the strongest when the disks are very close to each other, while the two successfully measured samples had large spacings of  $3\ \mu\text{m}$  and even  $5.4\ \mu\text{m}$ .

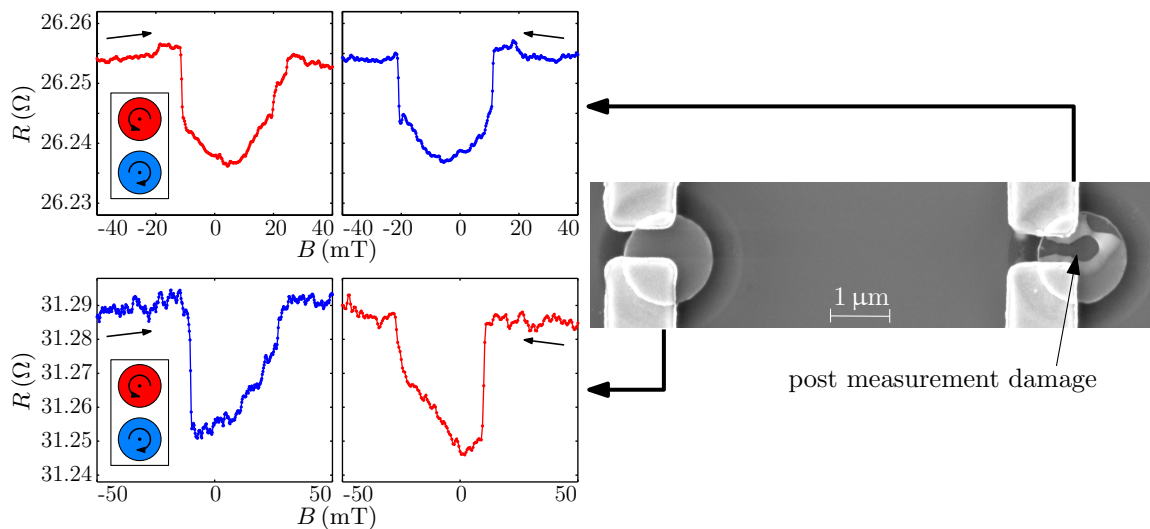


Figure 5.9: Anisotropic magnetoresistance measurements on the pair 1 of  $1.5\ \mu\text{m}$  disks prepared by the FIB trimming method. The disks have opposite circulations.

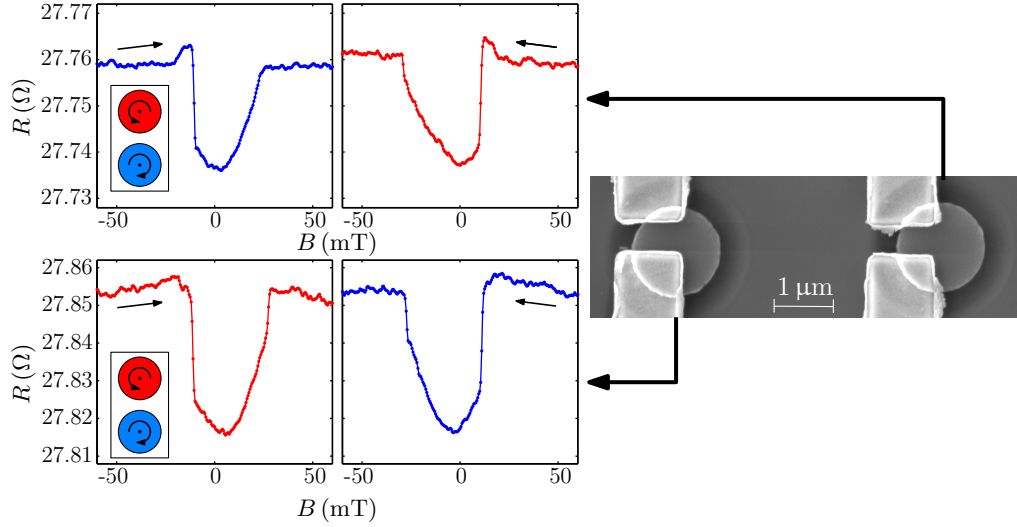


Figure 5.10: Anisotropic magnetoresistance measurements on the pair 2 of  $1.5\mu\text{m}$  disks prepared by the FIB trimming method. The disks have opposite circulations.

### 5.3 Magnetic force microscopy

Supporting magnetic force microscopy measurements were carried out using the Bruker Dimension Icon atomic force microscope. We used Olympus AC240TS probes sputter-coated with 30 nm of Co (measured on flat surface) to image the displaced vortex cores in an external magnetic field. The cores move in the perpendicular direction to the applied field, so the average magnetization component along the field is increased. Thus, we can distinguish between the two circulations based on the core displacement to the left or to the right, when the field is applied in the vertical direction. The sample was prepared by FIB trimming and consisted of pairs of  $1\mu\text{m}$  disks. The thickness was 30 nm and the interdisk spacing varied from  $0.4\mu\text{m}$  to  $2.5\mu\text{m}$ . The sample was saturated in the  $y$ -direction prior to the measurement. In the ten performed measurements (presented in Figure 5.11), it was found, that only three out of ten pairs have opposite circulations. This result brings a complementary proof against the concept of magnetostatic coupling in pairs of disks.

In the second experiment, we tried to prove the vortex nucleation mechanism in tapered disks as it was schematically shown in Figure 2.7. To reveal the vortex circulation, small cuts approx. 3 nm in depth were fabricated into the disks using a focused ion beam. The cuts break the flux-closure and leave surface charges that are detectable by the magnetic tip (in this case coated with 50 nm of Permalloy). This was studied on an array of  $1\mu\text{m}$  disks with 30 nm thickness. The topography image, along with a profile over one of the cuts, is shown in Figure 5.12. The profile shows, that the depth of the cut was approx. 3 nm. Prior to the measurement, the sample was saturated either to the left or to the right, while the tapered side of the disk was placed at the top (shown in the topography image). Then an image was acquired for each saturation left and right, with the white-black or black-white transition indicating the opposite vortex circulations. It was found that all of the disks follow the intuitive nucleation rule for asymmetric disks as it was presented in Figure 2.7.

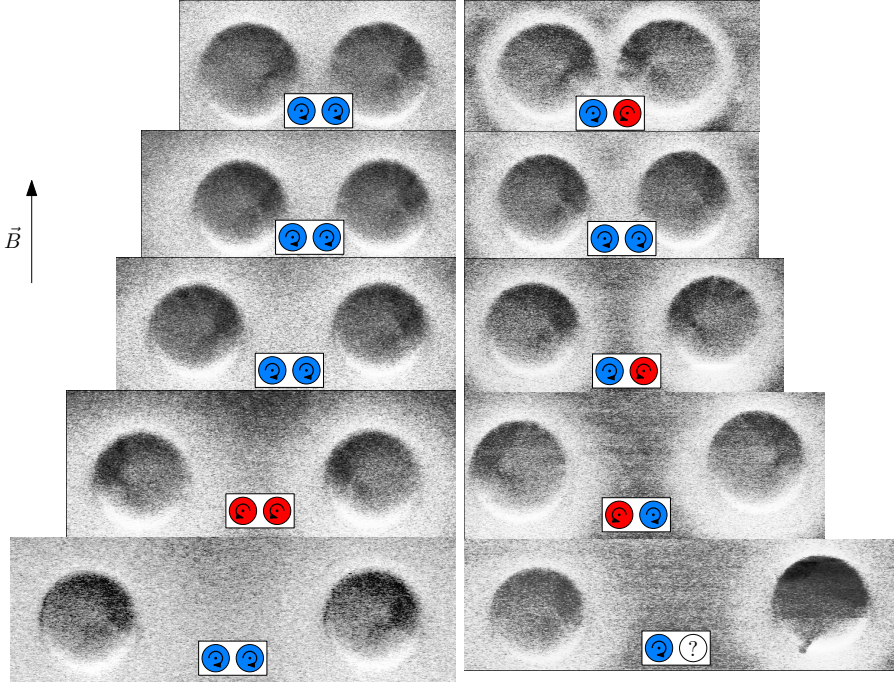


Figure 5.11: Magnetic force microscopy measurements of the disk circulation by imaging displaced vortex cores in an external magnetic field. Identical circulations were found in most cases, disproving the concept of magnetostatic coupling.

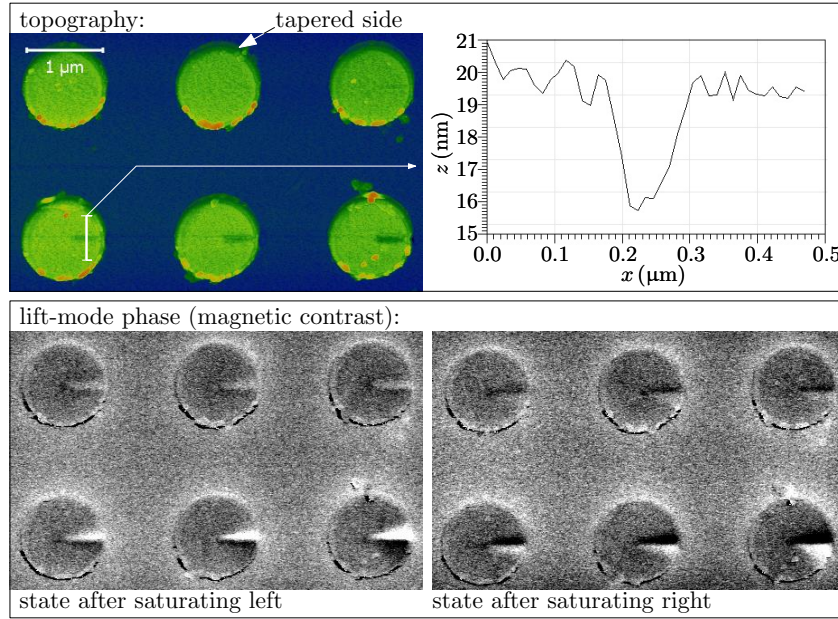


Figure 5.12: Measurements of vortex circulation on cuts fabricated by a focused ion beam. The profile of one of the cuts shows the depth approximately 3 nm. The nucleated vortex states were defined by the position of the tapered side of the disk at the top side. When the disks were saturated by a magnetic field pointing either left or right, the nucleated circulations were the same in one array and opposite for the two directions of saturation.

## 5.4 Magneto-optical Kerr effect

Hysteresis is an important characteristic proving the presence of the vortex states in the prepared disks. We measured hysteresis loops using the magneto-optical Kerr effect in a longitudinal configuration in a setup with He-Ne laser focused by a microscope objective. The sample was mounted on a piezo-stage to ensure precise placement of the spot. Two examples of hysteresis loops on 0.75, 1 and 4  $\mu\text{m}$  disks are presented in Figure 5.13. The smaller disks nucleated in a positive field and the measurements are in good agreement with the example shown in Figure 2.6 (Chapter 2) or with Simulation 3 (see Figure 5.1). The 4  $\mu\text{m}$  disk nucleated in a negative field (after passing the zero field) and the hysteresis loop shape is similar to Simulation 1 (see Figure 5.1).

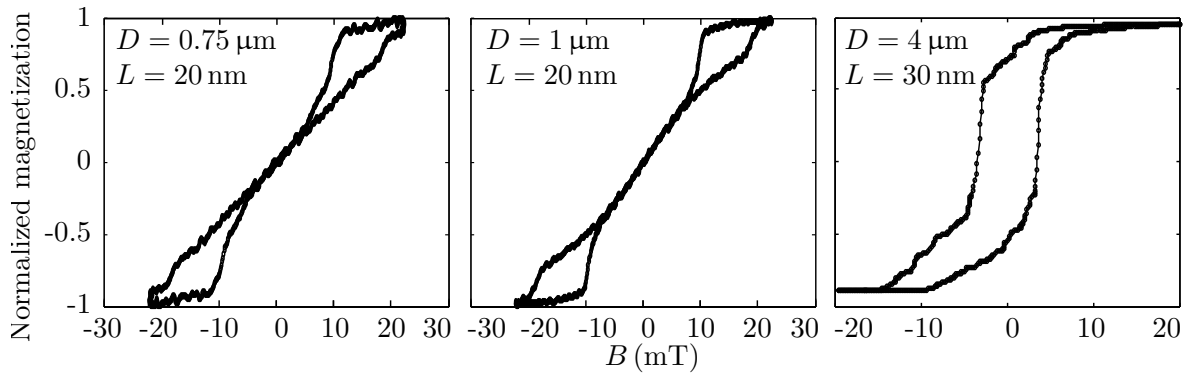


Figure 5.13: Hysteresis loops of Permalloy disks with diameters 0.75, 1 and 4  $\mu\text{m}$ .

Our simulations and measurements indicated that vortices nucleate through *S*-state, while some literature considers them to be spin instabilities obtained only in micromagnetic simulations [35]. Thus, we needed to prove the existence of the *S*-states, for which we used a magneto-optical Kerr effect instrument in a scanning configuration. Every spot is measured in two longitudinal configurations perpendicular to each other in order to obtain a vector map of magnetization in the whole scanning area.

Due to the optical resolution limit, we measured an 8  $\mu\text{m}$  disk, where we proved the presence of *S*-states and *C*-states in a real system. Simulations were carried out to be compared with the measured data, which is in good agreement, as presented in Figure 5.14. The measured *C*-state (left) shows that the magnetization is starting to bend when the field is being decreased until the *S*-state is formed (middle). The *S*-state has two cores (magnetized in the *z*-direction) that cannot be measured optically due to the resolution limit. But in the measured map, we can clearly see the two points, around which the magnetization is curling [Figure 5.14(b)], proving their presence. When the field is decreased, a vortex state is formed from the *S*-state [Figure 5.14(c)] and the corresponding peak in the anisotropic magnetoresistance disappears (see Figure 5.5 in Subsection 5.2.1).

Smaller objects are not easily measured optically due to the diffraction limit of light, meaning that similar experiment on  $\sim 1 \mu\text{m}$  disks would require different methods (for example SEMPA or XMCD). The used magneto-optical apparatus is closely described in [86] also



showing many other measurement results.

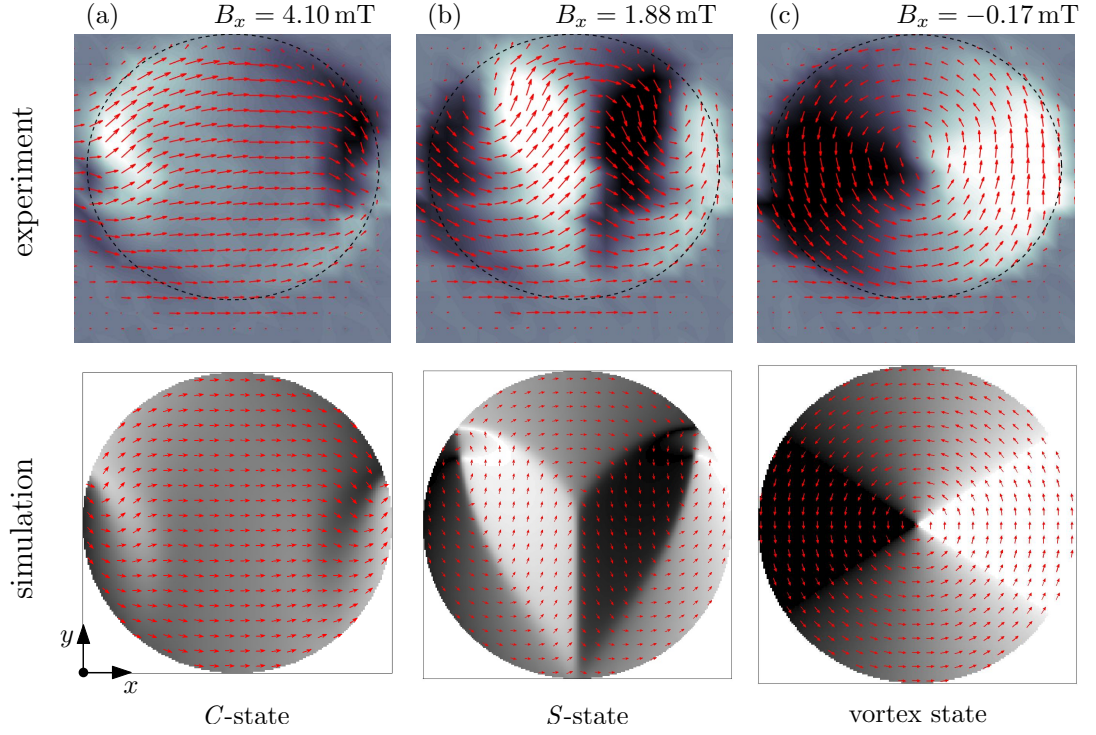


Figure 5.14: Comparison of micromagnetic simulations carried out in OOMMF with measured magnetization map in an 8 μm disk using a scanning Kerr microscope. The existence of a *C*-state [image (a)] and an *S*-state [image (b)] in a real disk was proven due to the fact that the simulations are in good agreement with the measurements. A measurement of the vortex configuration [image (c)] is shown as well. Courtesy of Lukáš Flajšman.

## Chapter 6

# Conclusion

In this work, we studied the process of the nucleation of vortex states in magnetic disks. First, we aimed at individual disks, where we studied the randomness of the spin circulation upon nucleation. Another research aspect involved the study of magnetostatic coupling in pairs of Permalloy disks. Until now, all research presented in literature was done only on arrays of disks (for example [49, 53]), where the magnetostatic coupling may play an important role while the arrays are densely packed. For this reason, measurements performed on a single disk (or a pair of disks) have a higher significance. There are several possibilities of how to measure the circulation of a single disk, but the only possible approach to providing a sufficient statistic is electrical measurement. In our study we used the anisotropic magnetoresistance and developed a setup for magnetoresistance measurements of the single disk. From the anisotropic magnetoresistance measurements we were able to obtain information about nucleation and annihilation fields, the sense of the spin circulation and the mechanism of vortex nucleation. By repeating the measurements for a single disk we were able to study the randomness of the nucleation process. This was necessary to prevent the defined vortex circulation switching, which is usually found in disks where asymmetry is present, and to ensure that the magnetostatic coupling would be the main effect conducting the vortex nucleations.

The used lithography methods played a key role in our project due to the necessity of a well defined geometry of the studied disks. Systematic experiments were carried out on single Permalloy disks with sizes ranging from  $4\text{ }\mu\text{m}$  down to  $1\text{ }\mu\text{m}$  while sample preparation methods were under development. The achieved level of randomness was only partially satisfactory, as only five out of more than one hundred of samples exhibited all possible states upon nucleation (clockwise and counter-clockwise sense of circulation for nucleations from both up and down saturations). Samples prepared by the lift-off process always exhibit a certain level of asymmetry as was explained in Chapter 3, which is the reason why they exhibit asymmetry-dependent nucleations in almost all cases. When a defined switching is desired, the asymmetry would be placed on a left or right side of the disk (relative to the external magnetic field direction). When the asymmetry is placed either on the top or the bottom of the disk, the nucleated states exhibit random behaviour, as was found in the case of the disk presented in Figure 5.6. An intuitive understanding of the effect is that the disk symmetry with respect to the direction of the magnetic field is preserved even for a tapered disk, but it

is not clear whether it would play a significant role for the magnetostatic coupling in pairs of disks. Studying the disk randomness as a function of the angle between the disk asymmetry and the applied magnetic field is considered to undergo further investigation.

The best results in terms of randomness were achieved from samples prepared by FIB trimming of the disk edges, compared to the disks that were prepared by lift-off. Using higher temperature than the room temperature also proved to help establish the randomness of the nucleation process.

More than one hundred samples were prepared, even while the experiments were delayed due to the initial struggle with the electrical contacting of the disks prepared by the FIB trimming process. The samples had repeatable resistances in order of  $k\Omega$ , that were too high compared to the samples prepared by lift-off with resistances of around  $20\Omega$ . This was later assumed to be caused by the SEM contamination, as the disks were imaged prior to FIB trimming. While the SEM observing was avoided during the lithographic process, the samples prepared by FIB trimming had comparable resistances with the samples prepared by lift-off.

The ion beam etching process is another possible sample preparation method, but it could not be properly tested due to difficulties with the mask preparation. On the other hand it is promising for future experiments as the installation of a new dedicated instrument or ion beam etching will take place this year as well as the installation of new sputtering and evaporator systems.

After many hours spent on studying the randomness of single disks, we prepared the desired pairs of disks. Previous single disk measurements did not predict very good chances of finding the opposite circulations as predicted by our theory of magnetostatic coupling, because we were not able to repeatedly fabricate samples exhibiting random nucleations of vortex states. Unfortunately the previous prediction was confirmed because we measured the opposite circulation for only two samples out of the total six functional samples. The other four samples either nucleated with the same circulation or exhibited a certain level of randomness. It was also verified using magnetic force microscopy measurements in an external magnetic field, where we measured the displaced positions of the vortex cores. Only three out of ten samples had opposite circulations, while the interdisk distance varied from  $0.4\mu\text{m}$  to  $2.5\mu\text{m}$ .

In summary, we carried out micromagnetic simulations as an initial input for magnetoresistance calculations using an original code to support our concept of the vortex circulation readout using the anisotropic magnetoresistance measurements. Then we successfully achieved an electrical readout of the vortex circulation by measuring the anisotropic magnetoresistance on many samples and therefore giving this method a good outlook as a simple and efficient method for a readout of the vortex circulation. Achieving random vortex circulations proved to be difficult and only partially satisfactory results were obtained. The concept of opposite circulations due to the magnetostatic coupling in a pair of disk was not verified. An unwanted geometrical asymmetry present in a majority of the samples most likely had a stronger effect on the vortex nucleation.



# List of abbreviations

<b>AMR</b>	anisotropic magnetoresistance
<b>APTES</b>	(3-Aminopropyl) triethoxysilane
<b>CEITEC</b>	Central European Institute of Technology
<b>DI</b>	deionized water
<b>DMI</b>	Dzyaloshinski-Moriya interaction
<b>FIB</b>	focused ion beam
<b>GPIB</b>	general purpose interface bus
<b>HSQ</b>	hydrogen silsesquioxane (negative e-beam resist)
<b>IBE</b>	ion beam etching
<b>IBS</b>	ion beam sputtering
<b>IPA</b>	isopropyl alcohol
<b>IPE BUT</b>	Institute of Physical Engineering, Brno University of Technology
<b>LLG</b>	Landau-Lifschitz-Gilbert equation
<b>MFM</b>	magnetic force microscopy
<b>MIBK</b>	methyl isobutyl ketone
<b>MOKE</b>	magneto optical Kerr effect
<b>OOMMF</b>	Object Oriented Micromagnetic Framework
<b>PMMA</b>	polymethyl methacrylate (positive e-beam resist)
<b>Py</b>	Permalloy
<b>RVM</b>	rigid vortex model
<b>SEM</b>	scanning electron microscope
<b>SEMPA</b>	scanning electron microscope with polarization analysis
<b>SIMS</b>	secondary ion mass spectroscopy
<b>SPM</b>	scanning probe microscopy
<b>TMAH</b>	tetramethylammonium hydroxide
<b>XMCD</b>	X-ray magnetic circular dichroism

# Bibliography

- [1] COEY, J. M. *Magnetism and Magnetic Materials*. Cambridge University Press, Cambridge, 2010.
- [2] MAXWELL, J. C. A dynamical theory of the electromagnetic field. *Philosophical Transactions of the Royal Society of London* 155 (1865), 459–513.
- [3] HUBERT, A., AND SCHÄFER, R. *Magnetic Domains - The Analysis of Magnetic Microstructures*. Springer, 1998.
- [4] CHAPPERT, C., FERT, A., AND VAN DAU, F. N. The emergence of spin electronics in data storage. *Nature materials* 6, 11 (2007), 813–23.
- [5] PARKIN, S. S. P. Data in the Fast Lanes of Racetrack Memory. *Scientific American* 300, 6 (2009), 76–81.
- [6] PRINZ, G. A. Magnetoelectronics applications. *Journal of Magnetism and Magnetic Materials* 200, 1-3 (1999), 57–68.
- [7] HERTEL, R. Magnetic nanostructures: vortex states à la carte. *Nature nanotechnology* 8, 5 (2013), 318–20.
- [8] UHLÍŘ, V., URBÁNEK, M., HLADÍK, L., SPOUSTA, J., IM, M.-Y., FISCHER, P., EIBAGI, N., KAN, J. J., FULLERTON, E. E., AND ŠIKOLA, T. Dynamic switching of the spin circulation in tapered magnetic nanodisks. *Nature nanotechnology* 8, April (2013), 341–6.
- [9] URBÁNEK, M., UHLÍŘ, V., LAMBERT, C.-H., KAN, J. J., EIBAGI, N., VAŇATKA, M., FLAJSMAN, L., KALOUSEK, R., IM, M.-Y., FISCHER, P., ŠIKOLA, T., AND FULLERTON, E. E. Dynamics and efficiency of magnetic vortex circulation reversal. *Physical Review B* 91, 9 (2015), 1–11.
- [10] BLUNDELL, S., AND THOULESS, D. *Magnetism in Condensed Matter*, vol. 71. 2003.
- [11] AHARONI, A. Upper bound to a single domain behavior of a ferromagnetic cylinder. *Journal of Applied Physics* 68, September (1990), 2892–2900.
- [12] HRABEC, A. *Domain wall dynamics in magnetic nanostructures : Effect of magnetic field and electric current*. Ph.D. thesis, Université de Grenoble, 2011.

- [13] STAÑO, M. *Characterization of magnetic nanostructures by magnetic force microscopy*. Master's thesis, Brno University of Technology, Faculty of Mechanical Engineering, 2014. Supervised by Ing. Michal Urbánek, Ph.D.
- [14] KRONMÜLLER, H., AND PARKIN, S. *Handbook of magnetism and advanced magnetic materials*. John Wiley & Sons, 2007.
- [15] AHARONI, A. *Introduction to the Theory of Ferromagnetism*. International Series of Monographs on Physics. Clarendon Press, 2000.
- [16] THIAVILLE, A., ROHART, S., JUÉ, E., CROS, V., AND FERT, A. Dynamics of Dzyaloshinskii domain walls in ultrathin magnetic films. *EPL (Europhysics Letters)* 100, 5 (2012), 57002.
- [17] ROHART, S., AND THIAVILLE, A. Skyrmion confinement in ultrathin film nanostructures in the presence of Dzyaloshinskii-Moriya interaction. *Physical Review B - Condensed Matter and Materials Physics* 88, 18 (2013), 1–8.
- [18] PIZZINI, S., VOGEL, J., ROHART, S., BUDA-PREJBEANU, L. D., JUÉ, E., BOULLE, O., MIRON, I. M., SAFEER, C. K., AUFFRET, S., GAUDIN, G., AND THIAVILLE, A. Chirality-induced asymmetric magnetic nucleation in Pt/Co/AlO<sub>x</sub> ultrathin microstructures. *Physical Review Letters* 113, 4 (2014), 047203.
- [19] VAŇATKA, M., ROJAS-SANCHEZ, J. C., VOGEL, J., BONFIM, M., THIAVILLE, A., AND PIZZINI, S. Velocity asymmetry of Dzyaloshinskii domain walls in the creep and flow regimes. Available from *arXiv*, <http://arxiv.org/abs/1504.00933>, 2015.
- [20] FERT, A., CROS, V., AND SAMPAIO, J. A. Skyrmions on the track. *Nature Nanotechnology* 8, 3 (2013), 152–156.
- [21] GILBERT, T. Classics in Magnetism A Phenomenological Theory of Damping in Ferromagnetic Materials. *IEEE Transactions on Magnetism* 40, 6 (2004), 3443–3449.
- [22] DONAHUE, M. J., AND PORTER, D. G. *OOMMF Users's Guide, Version 1.0*. National Institute of Standards and Technology, Gaithersburg, MD, 1999. Intragency Report NISTIR 6376.
- [23] VANSTEENKISTE, A., AND VAN DE WIELE, B. MuMax: A new high-performance micromagnetic simulation tool. *Journal of Magnetism and Magnetic Materials* 323, 21 (2011), 2585–2591.
- [24] FISCHBACHER, T., FRANCHIN, M., BORDIGNON, G., AND FANGOHR, H. A Systematic Approach to Multiphysics Extensions of Finite-Element-Based Micromagnetic Simulations: Nmag. *IEEE Transactions on Magnetism* 43, 6 (2007), 2896–2898.
- [25] ABERT, C., EXL, L., BRUCKNER, F., DREWS, A., AND SUESS, D. magnum.fe: A micromagnetic finite-element simulation code based on FEniCS. *Journal of Magnetism and Magnetic Materials* 345 (2013), 29–35.

- [26] BROWN, W. F. The Fundamental Theorem of Fine-Ferromagnetic-Particle Theory. *Journal of Applied Physics* 39, 2 (1968), 993.
- [27] LANDAU, L., AND LIFSHITS, E. on the Theory of the Dispersion of Magnetic Permeability in Ferromagnetic Bodies. *Phys. Zeitsch. der Sow.* 169, 14 (1935), 14–22.
- [28] ZHANG, S., GILBERT, I., NISOLI, C., CHERN, G.-W., ERICKSON, M. J., O'BRIEN, L., LEIGHTON, C., LAMMERT, P. E., CRESPI, V. H., AND SCHIFFER, P. Crystallites of magnetic charges in artificial spin ice. *Nature* 500, 7464 (2013), 553–7.
- [29] GOMEZ, R. D., LUU, T. V., PAK, A. O., KIRK, K. J., AND CHAPMAN, J. N. Domain configurations of nanostructured Permalloy elements. *Journal of Applied Physics* 85, 8 (1999), 6163.
- [30] ZHANG, Z., DUAN, H., WU, Y., ZHOU, W., LIU, C., TANG, Y., AND LI, H. Improving the adhesion of hydrogen silsesquioxane (HSQ) onto various substrates for electron-beam lithography by surface chemical modification. *Microelectronic Engineering* 128, 128 (2014), 59–65.
- [31] JÍRA, R. *Random number generator based on magnetic nanostructures*. Master's thesis, Brno University of Technology, Faculty of Mechanical Engineering, 2015. Supervised by Ing. Michal Urbánek, Ph.D., [in Czech].
- [32] BALAJKA, J. *Switching vortex chirality in magnetostatically coupled Permalloy nanodisks*. Master's thesis, Brno University of Technology, Faculty of Mechanical Engineering, 2013. Supervised by Ing. Michal Urbánek, Ph.D., [in Czech].
- [33] HENGSTMANN, T. M., GRUNDLER, D., HEYN, C., AND HEITMANN, D. Stray-field investigation on permalloy nanodisks. *Journal of Applied Physics* 90, 12 (2001), 6542.
- [34] RAHM, M., SCHNEIDER, M., BIBERGER, J., PULWEY, R., ZWECK, J., WEISS, D., AND UMANSKY, V. Vortex nucleation in submicrometer ferromagnetic disks. *Applied Physics Letters* 82, 23 (2003), 4110–4112.
- [35] GUSLIENKO, K., NOVOSAD, V., OTANI, Y., SHIMA, H., AND FUKAMICHI, K. Magnetization reversal due to vortex nucleation, displacement, and annihilation in submicron ferromagnetic dot arrays. *Physical Review B* 65 (2001), 1–10.
- [36] USOV, N., AND PESCHANY, S. Magnetization curling in a fine cylindrical particle. *Journal of Magnetism and Magnetic Materials* 118 (1993), L290–L294.
- [37] GUSLIENKO, K. Y., NOVOSAD, V., OTANI, Y., SHIMA, H., AND FUKAMICHI, K. Field evolution of magnetic vortex state in ferromagnetic disks. *Applied Physics Letters* 78, 24 (2001), 3848–3850.
- [38] SCHNEIDER, M., HOFFMANN, H., AND ZWECK, J. Magnetic switching of single vortex permalloy elements. *Applied Physics Letters* 79, 19 (2001), 3113–3115.

- [39] VAN WAEYENBERGE, B., PUZIC, A., STOLL, H., CHOU, K. W., TYLISZCZAK, T., HERTEL, R., FÄHNLE, M., BRÜCKL, H., ROTT, K., REISS, G., NEUDECKER, I., WEISS, D., BACK, C. H., AND SCHÜTZ, G. Magnetic vortex core reversal by excitation with short bursts of an alternating field. *Nature* 444, 7118 (2006), 461–4.
- [40] Magnetic vortex core reversal by excitation of spin waves. *Nature communications* 2 (2011), 279.
- [41] HERTEL, R., GLIGA, S., FÄHNLE, M., AND SCHNEIDER, C. Ultrafast Nanomagnetic Toggle Switching of Vortex Cores. *Physical Review Letters* 98, 11 (2007), 117201.
- [42] KAMMERER, M., WEIGAND, M., CURCIC, M., NOSKE, M., SPROLL, M., VANSTEENKISTE, A., VAN WAEYENBERGE, B., STOLL, H., WOLTERS DORF, G., BACK, C. H., AND SCHUETZ, G. Magnetic vortex core reversal by excitation of spin waves. *Nature communications* 2 (2011), 279.
- [43] CURCIC, M., VAN WAEYENBERGE, B., VANSTEENKISTE, A., WEIGAND, M., SACKMANN, V., STOLL, H., FÄHNLE, M., TYLISZCZAK, T., WOLTERS DORF, G., BACK, C. H., AND SCHÜTZ, G. Polarization Selective Magnetic Vortex Dynamics and Core Reversal in Rotating Magnetic Fields. *Physical Review Letters* 101, 19 (2008), 197204.
- [44] KIKUCHI, N., OKAMOTO, S., KITAKAMI, O., SHIMADA, Y., KIM, S. G., OTANI, Y., AND FUKAMICHI, K. Vertical bistable switching of spin vortex in a circular magnetic dot. *Journal of Applied Physics* 90, 12 (2001), 6548.
- [45] JAAFAR, M., YANES, R., PEREZ DE LARA, D., CHUBYKALO-FESENKO, O., ASENJO, A., GONZALEZ, E. M., ANGUITA, J. V., VAZQUEZ, M., AND VICENT, J. L. Control of the chirality and polarity of magnetic vortices in triangular nanodots. *Physical Review B - Condensed Matter and Materials Physics* 81 (2010), 1–7.
- [46] YAKATA, S., MIYATA, M., NONOGUCHI, S., WADA, H., AND KIMURA, T. Control of vortex chirality in regular polygonal nanomagnets using in-plane magnetic field Control of vortex chirality in regular polygonal nanomagnets using in-plane magnetic field. 2010–2013.
- [47] SCHNEIDER, M., HOFFMANN, H., OTTO, S., HAUG, T., AND ZWECK, J. Stability of magnetic vortices in flat submicron permalloy cylinders. *Journal of Applied Physics* 92, 3 (2002), 1466–1472.
- [48] VAVASSORI, P., GRIMSDITCH, M., METLUSHKO, V., ZALUZEC, N., AND ILIC, B. Magnetoresistance of single magnetic vortices. *Applied Physics Letters* 86 (2005), 1–3.
- [49] KONOTO, M., YAMADA, T., KOIKE, K., AKOH, H., ARIMA, T., AND TOKURA, Y. Formation and control of magnetic vortex chirality in patterned micromagnet arrays. *Journal of Applied Physics* 103, 2 (2008), 023904.

- [50] CHUNG, S.-H., MCMICHAEL, R. D., PIERCE, D. T., AND UNGURIS, J. Phase diagram of magnetic nanodisks measured by scanning electron microscopy with polarization analysis. *Physical Review B* 81, 2 (2010), 024410.
- [51] CHUNG, S.-H., PIERCE, D. T., AND UNGURIS, J. Simultaneous measurement of magnetic vortex polarity and chirality using scanning electron microscopy with polarization analysis (SEMPA). *Ultramicroscopy* 110, 3 (2010), 177–81.
- [52] NOVOSAD, V., GUSLIENKO, K., SHIMA, H., OTANI, Y., KIM, S., FUKAMICHI, K., KIKUCHI, N., KITAKAMI, O., AND SHIMADA, Y. Effect of interdot magnetostatic interaction on magnetization reversal in circular dot arrays. *Physical Review B* 65 (2002), 2–5.
- [53] IM, M.-Y., LEE, K.-S., VOGEL, A., HONG, J.-I., MEIER, G., AND FISCHER, P. Stochastic formation of magnetic vortex structures in asymmetric disks triggered by chaotic dynamics. *Nature communications* 5 (2014), 5620.
- [54] NAKANO, K., TANABE, K., HIRAMATSU, R., CHIBA, D., OHSHIMA, N., KASAI, S., SATO, T., NAKATANI, Y., SEKIGUCHI, K., KOBAYASHI, K., AND ONO, T. Real-time observation of electrical vortex core switching. *Applied Physics Letters* 102 (2013), 2–4.
- [55] HUANG, Y. S., WANG, C. C., AND ADEYEYE, A. O. Determination of vortex chirality using planar Hall effect. *Journal of Applied Physics* 100 (2006), 1–5.
- [56] SEGAL, A., AND GERBER, A. Core contribution to magnetotransport of ferromagnetic dots in vortex state. *Journal of Applied Physics* 111 (2012), 1–5.
- [57] CUI, X., HU, S., AND KIMURA, T. Detection of a vortex nucleation position in a circular ferromagnet using asymmetrically configured electrodes. *Applied Physics Letters* 105, 8 (2014), 082403.
- [58] WREN, T., AND KAZAKOVA, O. Anisotropic magnetoresistance effect in sub-micron nickel disks. *Journal of Applied Physics* 117, 17 (2015), 17E134.
- [59] NISHIMURA, N., HIRAI, T., KOGANEI, A., IKEDA, T., OKANO, K., SEKIGUCHI, Y., AND OSADA, Y. Magnetic tunnel junction device with perpendicular magnetization films for high-density magnetic random access memory. *Journal of Applied Physics* 91, 8 (2002), 5246.
- [60] NOVOSAD, V., FRADIN, F., ROY, P., BUCHANAN, K., GUSLIENKO, K., AND BADER, S. Magnetic vortex resonance in patterned ferromagnetic dots. *Physical Review B* 72, 2 (2005), 024455.
- [61] JUNG, H., CHOI, Y. S., LEE, K. S., HAN, D. S., YU, Y. S., IM, M. Y., FISCHER, P., AND KIM, S. K. Logic operations based on magnetic-vortex-state networks. *ACS Nano* 6, 5 (2012), 3712–3717.

- [62] KUMAR, D., BARMAN, S., AND BARMAN, A. Magnetic vortex based transistor operations. *Scientific reports* 4 (2014), 4108.
- [63] KIM, D.-H., ROZHKOVA, E. A., ULASOV, I. V., BADER, S. D., RAJH, T., LESNIAK, M. S., AND NOVOSAD, V. Biofunctionalized magnetic-vortex microdiscs for targeted cancer-cell destruction. *Nature materials* 9, 2 (2010), 165–171.
- [64] VITOL, E. A., NOVOSAD, V., AND ROZHKOVA, E. A. Microfabricated magnetic structures for future medicine: from sensors to cell actuators. *Nanomedicine (London, England)* 7 (2012), 1611–24.
- [65] KIMURA, T., OTANI, Y., MASAKI, H., ISHIDA, T., ANTOS, R., AND SHIBATA, J. Vortex motion in chirality-controlled pair of magnetic disks. *Applied Physics Letters* 90 (2007), 2–4.
- [66] BARMAN, A., BARMAN, S., KIMURA, T., FUKUMA, Y., AND OTANI, Y. Gyration mode splitting in magnetostatically coupled magnetic vortices in an array. *Journal of Physics D: Applied Physics* 43, 42 (2010), 422001.
- [67] JUNG, H., YU, Y.-S., LEE, K.-S., IM, M.-Y., FISCHER, P., BOCKLAGE, L., VOGEL, A., BOLTE, M., MEIER, G., AND KIM, S.-K. Observation of coupled vortex gyrations by 70-ps-time- and 20-nm-space-resolved full-field magnetic transmission soft x-ray microscopy. *Applied Physics Letters* 97, 22 (2010), 222502.
- [68] JUNG, H., LEE, K.-S., JEONG, D.-E., CHOI, Y.-S., YU, Y.-S., HAN, D.-S., VOGEL, A., BOCKLAGE, L., MEIER, G., IM, M.-Y., FISCHER, P., AND KIM, S.-K. Tunable negligible-loss energy transfer between dipolar-coupled magnetic disks by stimulated vortex gyration. *Scientific reports* 1 (2011), 59.
- [69] SUGIMOTO, S., FUKUMA, Y., KASAI, S., KIMURA, T., BARMAN, A., AND OTANI, Y. Dynamics of Coupled Vortices in a Pair of Ferromagnetic Disks. *Physical Review Letters* 106, 19 (2011), 197203.
- [70] SUGIMOTO, S., FUKUMA, Y., AND OTANI, Y. Manipulation of the excitation state of the coupled vortices in a pair of magnetic disks. *IEEE Transactions on Magnetics* 47, 10 (2011), 2951–2953.
- [71] SUKHOSTAVETS, O. V., GONZALEZ, J. M., AND GUSLIENKO, K. Y. Magnetic Vortex Excitation Frequencies and Eigenmodes in a Pair of Coupled Circular Dots. *Applied Physics Express* 4, 6 (2011), 065003.
- [72] ZHOU, W., AND WANG, Z. L. Scanning Microscopy for Nanotechnology: Techniques and Applications, 2007.
- [73] RAI-CHOUDHURY, P. *Handbook of Microlithography, Micromachining, and Microfabrication: Microlithography*. SPIE Optical Engineering Press, 1997.

- [74] HLADÍK, L. *Switching of spin vortices in magnetic nanodiscs*. Master's thesis, Brno University of Technology, Faculty of Mechanical Engineering, 2012. Supervised by Ing. Michal Urbánek, Ph.D. [in Czech].
- [75] BABOČKÝ, J. *Creation of plasmonic micro- and nanostructures by electron beam lithography*. Bachelor's thesis. Brno University of Technology, Faculty of Mechanical Engineering, 2012. Supervised by Ing. Michal Kvapil, [in Czech].
- [76] BABOČKÝ, J. *Optical response of asymmetric plasmonic structures*. Master's thesis, Brno University of Technology, Faculty of Mechanical Engineering, 2014. Supervised by Ing. Jan Čechal, Ph.D. [in Czech].
- [77] VAŇATKA, M. *Magnetic multilayers for spintronics applications*. Bachelor's thesis. Brno University of Technology, Faculty of Mechanical Engineering, 2013. Supervised by Ing. Michal Urbánek, Ph.D., [in Czech].
- [78] PAVERA, M. *Computer control of the deposition process*. Bachelor's thesis. Brno University of Technology, Faculty of Mechanical Engineering, 2009. Supervised by Ing. Michal Urbánek, Ph.D., [in Czech].
- [79] HRABEC, A. Personal communication, Brno, March 2015.
- [80] URBÁNEK, M., UHLÍŘ, V., BÁBOR, P., KOLÍBALOVÁ, E., HRNČÍŘ, T., SPOUSTA, J., AND SIKOLA, T. Focused ion beam fabrication of spintronic nanostructures: an optimization of the milling process. *Nanotechnology* 21, 14 (2010), 145304.
- [81] BARMAN, A., WANG, S., MAAS, J. D., HAWKINS, A. R., KWON, S., LIDDLE, A., BOKOR, J., AND SCHMIDT, H. Magneto-optical observation of picosecond dynamics of single nanomagnets. *Nano letters* 6, 12 (2006), 2939–44.
- [82] TUPTA, M. A. Ac versus dc measurement methods for low-power nanotech and other sensitive devices, 2007. Available from <http://www.keithley.com/products/dcac/sensitive/acdc/?mn=62212182A>, [Accessed 2015-05-17].
- [83] Atomic force microscopy (afm), 2014. Available from <http://www.farmfak.uu.se/farm/farmfyskem/instrumentation/afm.html>, [Accessed 2015-05-10].
- [84] TURČAN, I. *Variable field magnetic force microscopy*. Bachelor's thesis. Brno University of Technology, Faculty of Mechanical Engineering, 2015. Supervised by Ing. Michal Urbánek, Ph.D., [in Czech].
- [85] QIU, Z. Q., AND BADER, S. D. Surface magneto-optic Kerr effect. *Review of Scientific Instruments* 71, 3 (2000), 1243.



- [86] FLAJŠMAN, L. *Vectorial Kerr magnetometry*. Master's thesis, Brno University of Technology, Faculty of Mechanical Engineering, 2015. Supervised by Ing. Michal Urbánek, Ph.D.
- [87] FLAJŠMAN, L. *Design of the apparatus for the measurement of the magnetic properties of the micro and nanostructures*. Bachelor's thesis. Brno University of Technology, Faculty of Mechanical Engineering, 2013. Supervised by prof. Jiří Spousta, Ph.D., [in Czech].